HIMAC-090

Effects of Field Distortions in IH-APF Linac for a Compact Medical Accelerator

Valery Kapin, Yoshiyuki Iwata, Satoru Yamada

July, 2004

National Institute of Radiological Sciences
9-1 Anagawa 4-chome, Inage-ku, Chiba 263-8555, JAPAN

Effects of Field Distortions in IH-APF Linac for a Compact Medical Accelerator

Valery Kapin*, Yoshiyuki Iwata, Satoru Yamada

Department of Accelerator Physics and Engineering, National Institute of Radiological Sciences,
4-9-1 Anagawa, Inage-ku, Chiba 263-8555, JAPAN

Abstract: The project on developing compact medical accelerators for the tumor therapy using carbon ions has been started at the National Institute of Radiological Sciences (NIRS). Alternating-phase-focused (APF) linac using an interdigital H-mode (IH) cavity has been proposed for the injector linac. The IH-cavity is a doubly ridged circular resonator loaded by the drift-tubes mounted on ridges with supporting stems. The effects of intrinsic and random field distortions in a practical design of the 4-Mev/u 200-MHz IH-APF linac are considered. The intrinsic field distortions in the IH-cavity are caused by an asymmetry of the gap fields due to presence of the stems and pair of ridges. The random field distortions are caused by drift-tube misalignments and non-regular deviations of the gap voltages from programmed values. The RF fields in the IH-cavity have been calculated using Microwave Studio (MWS) code. The effects of field distortions on beam dynamics have been simulated numerically.

The intrinsic field distortions are negligible for this IH-APF linac. The random field distortions cause a serious degradation of the beam transmission. The levels of permissible errors for the drift-tube longitudinal and transversal displacements are about ±200 μm and ±100 μm, respectively. The fluctuations of the gap voltages should be minimized to the levels of about ±3%. At this level of tolerances the beam transmission is decreased about 10 % (standard-deviation value) comparing to the beam transmission for the ideal structure. A possible way to relax the level of permissible errors is to shorten the IH-APF structure by increasing the transition energy between RFQ and IH-APF linacs. A modified linac layout is proposed and discussed.

---

*On leave from Moscow Engineering Physics Institute;
e-mail: kapin@mail.ru

1. Introduction

The progress of the radiation therapy in clinical cancer treatments with carbon ions at the Heavy Ion Medical Accelerator (HIMAC) facility [1] of the National Institute of Radiological Sciences (NIRS) encourages developments of a small-sized therapy system aiming to spread the carbon therapy for local hospitals in the whole country [2]. The project on developing compact and reliable medical accelerators for the tumor therapy using carbon ions has been started at the Division of Accelerator Physics and Engineering of NIRS [3]. The accelerator complex for this compact facility (Fig. 1,a) consists of two ECR ion sources with permanent magnets, an injector linac cascade with the ion energy of 4 MeV/n, a synchrotron ring with the maximum energy of 400 MeV/n and beam delivery system for three treatment rooms. The research and design works for the new facility have been started from April 2004.

The linac cascade (Fig.1,b) consists of the 600 keV/u four-vane cavity with radio-frequency-quadrupole (RFQ) focusing and the 4 MeV/u inter-digital H-type (IH) drift-tube (DT) cavity with alternating-phase focusing (APF). Both structures operate at the RF frequency of 200 MHz. Design considerations and preliminary calculation results for this injection linac has been already presented in our reports [4-6]. Since beam intensities of ECR carbon ion sources are near their limits, it is important to preserve high beam transmission abilities of the linac. It has been shown, that in such linac layout, the current transmission of a carbon beam can reach up to 90-100%.

Since a design technology of RFQ is well known and proved both theoretically and experimentally, including HIMAC RFQ [7], our efforts are mainly devoted to the IH-APF structure. In previous studies [4-6], it has been already adopted, that in order to minimize the length of the IH-APF structure and to keep its focusing abilities, it is advantageous to use a gradient-type of the gap-voltage distribution along the structure and to alternate the synchronous phase along the structure with an increasing period (from 10 up to 20 gaps per period). Principally, the length of the 4Mev/u IH-APF can be minimized as small as about 2 m, if one is neglecting a beam quality. However, to provide a good beam quality, the length of IH-APF should be about 3 m. The beam dynamics calculations have been performed for a practical design of the 4-Mev/u 3.2 m long IH-APF linac [8] and are presented in the next section.

The beam dynamic simulations for the IH-APF structure with ideal fields having a pure axial symmetry and programmed voltage distributions have shown satisfactory results.

However, a real IH-APF structure has several kinds of the field distortions, which can strongly affect on the beam quality. In this report, a practical design of the IH-APF linac [8] is explored with possible field distortions. Let's distinguish intrinsic and random field distortions. The former are inherent to the structure and exist even in a structure with an ideal geometry, and the latter are caused by the errors arising at the stage of the mechanical alignment and RF tuning of the structure.

The intrinsic field distortions in IH-cavity have been analyzed using computer simulations of RF fields with Microwave Studio (MWS) code [9]. The IH-cavity is doubly ridged circular resonator loaded by the drift-tubes mounted on ridges with supporting stems. The intrinsic field distortions in IH-cavity are mainly caused by the asymmetry of the gap field due to presence of the drift-tube supporting stems and pair of ridges. Many geometrical configurations of the ridges and stems are known and used in a practice [10-12]. It is known, that the shapes of the ridges and stems affect on the RF performances of the structure and magnitudes of field distortions. We have performed a quite comprehensive study of different configurations of the ridges and stems using MWS-code in order to estimate their influence quantitatively. The results are presented in the third section.

The random field distortions are caused by drift-tube misalignments and non-regular deviations of the voltage distribution from a programmed law. It is a serious problem for any kind of strong-focusing linacs [13-15], and especially for APF linacs, which have relatively weak focusing forces and therefore are very sensitive to the any field perturbations [16-18]. Although there are analytical methods for estimations of the effects due to random field distortions, a numerical simulation of beam dynamics provides more reliable results [18].

The effects of the intrinsic and random field distortions on beam dynamics have been simulated numerically with DYN1 code written by V. Kapin. The results are presented and discussed in the forth section. The level of permissible errors for the drift-tube longitudinal and transversal displacements is about ±200 μ m and ±100 μ m, respectively. The fluctuations of the gap voltages should be minimized to the levels of about ±3%.

These tolerance levels are achievable with a modern technology [1]. However, it requires time-consuming procedures for a careful mechanical assembling and RF tuning. It may results in a difficult and expensive manufacturing technology, which is not appropriate for several batch-produced linacs. A possible way to relax the level of permissible errors is to shorten the IH-APF structure by increasing the transition energy between RFQ and IH-APF linacs. A modified linac layout is outlined and discussed in the last section.

2. Beam dynamics with non-distorted fields

The IH-structure is a kind of a π - mode multigap accelerating structure, where a time-alternating RF voltage is applied to a sequence of drift-tubes whose lengths tend to increase with increasing particle velocity. The electrical fields in the gaps between drift-tubes act to accelerate the particles. It is usual to consider the multigap drift-tube linac as a sequence of unit cells. It is assumed, that the cell boundaries are located at the electrical centers of successive drift-tubes, where by symmetry the electric field has only a longitudinal component. Thus, the cell consists of a gap and two halves of adjoining drift-tubes.

The beam dynamics calculations have been performed for a practical design of the 4-Mev/u 3.2 m long IH-APF linac [8]. This design is approved for a cold model of IH-structure. The carbon ions $_{12}C^{+4}$ are accelerated from the injection energy of 600 keV/u. The bravery factor for the Kilpatrick limit is about 1.6. In this linac design, a gradient type of voltage distribution along the tank is used, while the gap voltage is approximately proportional to the relative velocity of the synchronous particle, $U_{\rm g} \propto \beta_{\rm s}$. The cell table is given in Table 1, where L is the total length at the exit of the i-th cell, L_1 is the distance between the cell entry and the gap entry, $L_{\rm g}$ is the gap length, L_2 is the distance between the gap exit and the cell exit, $U_{\rm g}^0$ is the instantaneous peak voltage along the cell axis ($r = 0$), ϕ_s is the synchronous phase. The cell length can be derived from these data as $L_{\rm cell} = L_1 + L_{\rm g} + L_2$.

The beam dynamics has been simulated with DYN1-code, which computes the trajectories of the particles through the linac cell-by-cell, while the motion equations within every cell are solved by the numerical integration using the 4-th order Runge-Kutta method. The electrical fields within every cell have been be derived in the electrostatic approach, which is usually used for low-energy linacs [14]. The electrical field is calculated as a gradient of the potential, $\vec{E} = -\nabla U$. The potential inside the cylindrical volume of the accelerating cell with the aperture radius a is presented as Fourier-Bessel series with the period $L = \beta_{\rm s}\lambda$:

$$U(r,z) = U_0 + \sum_j \left\{ I_0\left(\frac{2\pi j}{L} r\right)\left[A_j \cos\left(\frac{2\pi j}{L} z\right) + B_j \sin\left(\frac{2\pi j}{L} z\right)\right] \Big/ I_0\left(\frac{2\pi j}{L} a\right)\right\}. \quad (2\text{-}1)$$

Using a given potential distribution on the cylindrical surface at $r = a$, the coefficients of the series can be calculated using the numerical harmonical analysis. The potential values at $r = a$ can be calculated using some numerical code, e.g., POISSON code [19]. Examples of the field calculations with POISSON code have been presented in the previous report [4]. It has been shown, that for the potential distributions along the accelerating cells at the aperture radius $r = a$ calculated with the POISSON code are well approximated by the linear dependence. For fast beam dynamics simulations, the DYN1 code uses a linear approach to the potential distribution on the cylindrical surface $r = a$. It is quit usual approach in linac codes [20, 21].

The voltages in the cell-table (Table 1) are the voltages on the cell axis, U_{g}^{0} at $r = 0$. Due to the effect of voltage depression in a sequence of alternatively charged drift-tubes, the voltage between drift-tube surfaces, $U_{\mathrm{g}}^{\mathrm{DT}}$ is larger than voltage on the cell axis, U_{g}^{0}. Since the fields in cells are calculated from the potential distribution on the cylindrical surface at $r = a$, the DYN1 code uses voltages between drift-tube surfaces $U_{\mathrm{g}}^{\mathrm{DT}}$ as an input parameter. In order to derive the drift-tube voltages $U_{\mathrm{g}}^{\mathrm{DT}}$ from the given in the cell-table voltages U_{g}^{0} the following procedure has been adopted.

At first step, the voltages on the cell axis U_{g}^{0} have been used as the drift-tube voltages, $u_{\mathrm{g}}^{\mathrm{DT}}$. It allows to calculate in the linear approximation the corresponding voltages on axis, u_{g}^{0}, and the voltage depression factor as $\Psi_U = u_{\mathrm{g}}^{0} / u_{\mathrm{g}}^{\mathrm{DT}}$. The Figure 2,a shows voltage $u_{\mathrm{g}}^{\mathrm{DT}}$ and u_{g}^{0}, and the factor Ψ_U as functions of the cell number. On the second step, the drift tube voltages have been calculated as $U_{\mathrm{g}}^{\mathrm{DT}} = U_{\mathrm{g}}^{0} / \Psi_{\mathrm{U}}$. The Figure 2,b shows the restored voltage $U_{\mathrm{g}}^{\mathrm{DT}}$ and U_{g}^{0}, and the voltage depression factor Ψ_U as functions of the cell number. One can see, that of voltage depression is quite considerable (up to 12 %), and its minimum values repeated along the structure at the locations of the short drift-tube. The effect of voltage depression cannot be neglected and, it is taken into account in DYN1 code even with a linear approach for the potential distribution on the cylindrical surface at $r = a$.

To avoid time-consuming numerical calculations of Fourier-Bessel series, we used a paraxial approximation to the potential. In paraxial approximation, the axially symmetrical potential is expressed by the series

$$U(r,z) \cong U(0,z) - \frac{r^2}{2^2} U''(0,z) + \ldots + \frac{(-1)^n}{(n!)^n} \left(\frac{r}{2}\right)^{2n} U^{(2n)}(0,z), \qquad (2\text{-}2)$$

where the function $U(0,z)$ is the potential distribution on the cell axis at $r = 0$. This function is calculated using a cubic-spline interpolation for the values of $U(0,z_n)$, which has been calculated from the above Fourier-Bessel series for potential (2-1).

The longitudinal acceptance of the IH-APF linac calculated for axial particles ($r = 0$) is presented in Figure 3,a. The dependence of the longitudinal acceptance on the relative voltage amplitude in IH-APF tank has been studied. The calculations have showed that the longitudinal acceptance preserves its area without an essential reduction for the relative voltage amplitudes within the interval [0.98, 1.10]. The longitudinal emittance of the injected particles is presented in Figure 3,a. It corresponds approximately to the longitudinal phase-space of the beam after matching section located between RFQ and IH-APF. Phase space correspond to the divergent beam bounded within the RF phases $\varphi_{\mathrm{rf}} \in$ [-62°, -17°] and within the relative velocities $\beta \in$ [3.57%, 3.63%]. It is seen that area occupied by the injection emittance is much less than total area of the longitudinal acceptance for axial particles.

The beam dynamic calculations have been performed for the randomly distributed particles. The number of the particles in simulations is equal to N_{particle} =1000. In the transverse phase spaces, particles are uniformly distributed within the upright ellipces on the (x, x') and (y, y') phase spaces. The ellipce are determined by the following formula:

$$\varepsilon_x = \gamma_x \cdot x^2 + 2\alpha_x \cdot x \cdot x' + \beta_x \cdot x'^2 \qquad (2\text{-}3)$$

with the parameters γ_x =2.0 rad/m, α_x =0.5 m/rad and α_x =0. The phase-space ellipses correspond to the transversal phase-spaces of the beams after the matching section located between RFQ and IH-APF.

The dependencies of the beam transmission T_{beam} for different values of ε_x are shown in the Figure 4,a. The beam transmission is rapidly drop down when the value of ε_x increases. For this linac the lower permissible transmission threshold is about 50 %. Since RFQ may lose up to 10 % of the injected particles, the beam transmission of the IH-APF tank must be higher than 60 %. Therefore, the value of ε_x for transverse emittance of the injected beam should be lower than ε_x=18.0 $\mathrm{mm} \times \mathrm{mrad}$.

Note, that the value of ε_x =18.0 $\mathrm{mm} \times \mathrm{mrad}$ corresponds to the phase-space area occupied by all particles after the matching section between RFQ and IH-APF [5]. It is known, that the value of beam transmission depends on the kind of the phase-distribution of injected particles. In the above calculations, we have used a uniform distribution. However, the actual phase-space distributions after the matching section have a high-dense core and a low-dense halo. This is one of possible reasons explaining higher transmission values obtained in report [5].

The calculation results for a smaller value of ε_x =8.0 mm$\times$mrad provide a more appropriate value of the beam transmission T_{beam} =92 %. The longitudinal and transverse beam emittances at the exit of the IH-APF linac are shown in Figure 4,b and Figure 4,c, respectively. The transverse emittance of the output beam occupies area $22\,\pi \times \text{mm} \times \text{mrad}$. The phase portrait of the beam in the longitudinal phase-space has a dense core with width of about 25 degrees and a long tail is smearing over about 50 degrees. The energy spread is about $\Delta W/W \approx \pm 0.7\%$. It is still higher, than the requirements for the energy spread of output beam, which is $\Delta W/W \leq \pm 0.4\%$.

We should note, that these data have been obtained in the paraxial approximation for the fields (2-2) and using a linear approach for the potential distribution on the cylindrical surface at $r = a$. More precise values should be calculated with a full Fourier-Bessel series (2-1) and with a potential distribution calculated with POISSON-code on the cylindrical surface $r = a$.

3. Performances of IH-cavity at different shapes of the ridges and the drift-tube supporting stems

The IH cavity is widely used for drift-tube linac. It consists of the tank and one, two or four ridges, which act as main resonance elements. The drift-tubes are connected to the ridges by the supporting stems. In our IH-APF linac design, the doubly ridged circular resonator is used. The schematic drawing of an IH-cavity is shown in Figure 5,a.

Many geometrical configurations of the ridges and stems are known and can be used [10-12]. The geometrical features the ridges and stems may affect on the RF performances of the structure and magnitudes of field distortions. Some special configurations are aimed to eliminate dipole components of the accelerating field, to reduce the surface current density, or to increase the shunt-impedance.

Let's estimate their influence quantitatively, using MWS-code. Table 2 lists the parameters of an interest, which can be observed with MWS-code. According to the cell-table of the IH-APF linac (see Table 1), the cell length L_{cell} varies from about 22 mm to 66 mm.

The three typical cell lengths are considered, namely 22 mm, 44 mm, and 66 mm. The basic dimensions of IH-cavities with constant cell lengths are listed in Table 3.

At the first stage, relatively short 6-gap structures have been explored. The short structures require smaller computational power and allow faster evaluations of wanted effects in comparison with the long structures. However, there is a qualitative difference in electromagnetic performances of short and long IH-cavities. The behavior of our IH-APF structure is more adequately simulated by a long IH-cavity. The performances of a long IH-structures have been refined with two 21-gap structures (Fig. 5,b), which have different cell lengths L_{cell} =22 mm and L_{cell} =44 mm.

3.1 Variation of the ridge shape (the angle of side surface)

The ridges of IH-cavity serve as important resonant elements. Ridges with trapezoidal and rectangular cross-sections are known. We have examined the influence the ridge cross-section on the performances of the IH-cavities with trapezoidal cross-section of the ridges. The independent parameter is the angle of the side surface α_{R} , while a zero angle corresponds to the rectangular cross-section. Figure 5,b shows the 21-gap structure with trapezoidal ridge.

The results of the calculations are collected in Table 4. The magnitude of the dipole field is practically independent from the ridge angle α_{R}. The dependencies of the quality factor Q_0, resonance frequency f_0 and the shunt-impedance R_{sh} on the ridge angle α_{R} are shown in Figures 6 and 7. The dependences for the 6-gap IH-cavity with the tank radius R_{tank} =180 mm and for the 21-gap IH-cavities with the tank radius R_{tank} =150 mm both having the same cell length L_{cell} =22 mm are shown in Fig. 6,a and Fig.6,b, respectively. These structures have short drift-tubes and use conical stems (see Table 3). The dependences for two 6-gap IH-cavities with the cell lengths L_{cell} =44 mm and L_{cell} =66 mm both having the same tank radius R_{tank} =180 mm are shown in Fig. 7,a and Fig. 7,b, respectively. These structures use cylindrical stems (see Table 3).

In the above Figures, the values of Q_0, f_0, and R_{sh} are all increased with increasing the ridge angle α_{R}. It is looked as a weak improvement in the shunt impedance (3-10 %) and Q-factor with increasing angle α_{R}. However, at the same time the resonance frequency is also increased. For this reason, it is interesting to check the shunt impedance behavior at the same resonance frequency.

Practically, the resonance frequencies of IH-cavities with different ridges can be adjusted to the same value by the variation of the tank radius. The calculated RF parameters of three 21-gap IH-cavity with cell length L_{cell} =44 mm (the average value of our IH-APF linac) and three different tank radii are presented in the Table 5. The IH-cavities with the tank radius R_{tank} =170 mm, R_{tank} =180 mm, and R_{tank} =190 mm have the same resonance frequency (f_0 =200 MHz, f_0 =201 MHz, f_0 =201 MHz, respectively) at the ridge angles α_R =0°, α_R =20°, and α_R =35°, respectively. The corresponding values of the shunt impedance are R_{sh} =648 kΩ, R_{sh} =630 kΩ, and R_{sh} =642 kΩ, respectively. Thus, variations of the ridge angle α_R does not influence on the shunt-impedance of the IH-cavity.

The similar conclusion has been obtained about 20 years ago by the INS group [11] during experimental studies of the "wing tuner", with which allows to tune the voltage distribution along the whole IH-structure. The "wing tuner" acts similar to a variation of the ridge angle α_R. They have concluded: "the quality factor and the shunt impedance remained practically unchanged by these inductive tuning elements".

This interesting feature can be used for tuning the gradient type of the voltage distribution without a degradation of the shunt impedance. Figure 8,a shows the IH- cavity with monotonic decreasing the ridge angle along the whole structure. The electrical field distribution along the structure is shown in Figure 8,b. This IH-cavity has the constant cell length; therefore the voltage distribution has the same dependence as the electrical field. To refine the voltage distributions, the ridges are cut at the both ends of tank. However, this method can be effective for relatively short cavities. The cold model of IH-APF linac has length of 3.2 m, and another method for arranging the gradient-type of the voltage distribution is used. The cavity radius is changed in 4 steps [8].

3.2 Effects of the stem profile

The stem configurations have been studied in the several laboratories [10-12]. It is known that a concentration of the surface current on the supporting stems tends to cause excess of power loss and overheating the stem surface. The power dissipation on the stem surfaces is estimated to relatively large.

The experimental study of effects of stem profile had been performed by the INS group [11]. A simple equivalent-circuit model of the IH-cavity assuming uniform current distributions on conductors predicts a strong dependence of the shunt impedance. The tested stems had triangular and cylindrical profiles. The INS measurements showed that Q-values of the different stem profiles lie within the error. The qualitative explanation of such behavior: "the Rf resistance of the triangular stem is not improved so much because of the inhomogeneous current density on the stem surface". Our calculations with the MWS-code are consistent with the conclusions by INS group.

The results of our calculations are presented in Tables 6 and 7. Three cavities with conical, cylindrical and triangular stems have been calculated: two cavities with L_{cell} =22 mm, namely the short 6-gap and the long 21-gap cavities, and the short 6-gap cavity with L_{cell} =44 mm. The stem geometries are presented in Figure 9. The conical stems (Fig.9,a) with upper diameter d_1 =3.0 mm and triangular stems (Fig.9,c,d) with s_{vert} =3.0 mm are used in IH-cavities with short drift tubes (L_{cell} =22 mm) and cylindrical stems (Fig.9,b) with diameter d_{c} =9.0mm and triangular stems (Fig.9,e,f) with s_{vert} =9.0mm in IH-cavities with long drift tubes (L_{cell} =44 mm). The triangular stems are reshaped by changing the parameter ξ_{s} . Figures 9,c,e and Figures 9,d,f show triangular stems at ξ_{s} =0 mm and at arbitrary values of ξ_{s}, respectively. The data in Tables 7 and 7 demonstrate that there is no essential difference in the shunt impedance and quality factor for different stem geometries. The relative magnitude of the dipole voltage V_y/V_{g} is higher for large gaps and increases with increasing parameter ξ_{s} for triangular stems. For cylindrical stems V_y/V_{g} is equal to 2 % and 6 % for the gap lengths L_{g} =10 mm (L_{cell} =22 mm) and L_{g} =20 mm (L_{cell} =44 mm), respectively.

The pictures of the surface current distributions are shown in Figure 10 for cylindrical and conical stems. It is seen that there is a considerable concentration of the surface current on the supporting stems. The surface currents are uniformly distributed along cylindrical stems, and concentrated near drift-tubes for conical stems. There can be overheating the stem surface, if the structure operates at high levels of duty factors, when average power losses are high. The duty factor for our IH-APF cavity is lower then 0.1 %, and average power losses in the cavity are less 500 W. At such levels of RF power, the effects of stem overheating can be neglected. Therefore, simple stems with cylindrical shape have been chosen.

4. Effects of intrinsic and random errors

It is known any accelerating structure has some errors [13-15]. There are systematic and random errors [14]. Systematic errors have no random nature, they related to the errors in calculations or measuring of parameters. The intrinsic field distortion due to presence drift-tube supporting stems is an example of the possible systematic errors. Here, other systematic errors arising due to a used calculation approach for generation and analysis of linac are not considered. However, one should keep in mind that an approximate calculation method provides systematic errors and real beam parameters will differ from calculated ones.

The intrinsic field distortions in the IH-cavity mainly appear as dipole fields acting in the vertical direction. Figure 8 shows an example of the dipole field distribution (E_y -component) along the cavity. The dipole fields in the gaps are in-phase. Since drift-tube lengths are calculated for π -mode of the gap fields, the dipole fields act in opposite directions in neighboring gaps and their sum effects are almost compensated. Due to regular nature of the intrinsic fields, its integral action along the whole linac is negligible.

For the beam dynamics calculations with DYN1 code, the longitudinal distribution of the dipole fields within unit cells has been approximated by the known distribution of the axially-symmetrical gap field, while an amplitude of the dipole field in gaps has been expressed using the ratio between amplitudes of the dipole field and the accelerating field, $E_y^{\max} \big/ E_z^{\max}$, which has been approximated by the linear law $E_y^{\max} \big/ E_z^{\max} = 0.02 + 0.028 \cdot z$. The ratio $E_y^{\max} \big/ E_z^{\max}$ rises from 2 % to 11 % along the linac length. The beam dynamics simulations for the beam transmission in the presence of the dipole field have not shown any serious effects, while the beam transmission has not changed at all.

Further, let's consider only random field distortions. These errors are randomly distributed in time and space. Even relatively small errors may essentially deteriorate the beam quality, because they interact with beam many times. The drift-tube linacs with strong focusing are extremely sensitive to random errors in positions and strength of the lens elements [13-15]. It is especially a serious problem for APF structures, which have relatively weak focusing forces [16-18]. In APF linac, the random field distortions are caused by drift-tube misalignments and non-regular deviations of the voltage distribution from programmed law. Although there are analytical methods for estimations of the effects of random errors [13-15,17], a numerical simulation of beam dynamics provides more reliable results [18].

The effects of the random field distortions on beam dynamics have been simulated numerically with DYN1 code. The number of random experiments in every case is equal to $n = 100$. The dependence of the beam transmission T_{beam} on the emittance parameter ε_x has been explored at different levels of random errors for voltage distribution and drift-tube positions. For ideal fields this dependence has been calculated in the section 2 (Fig.4,a). For a simple statistical analysis of the obtained results, we have calculated the mean value and the standard deviation of the beam transmission given by the following formulae:

$$\overline{T}_{\text{beam}} = \sum\nolimits_{i=1}^{n} T_{\text{beam}}^{i} \Big/ n \,, \quad T_{\text{beam}}^{\text{st.dev}} = \sqrt{\frac{1}{n-1}\sum_{i=1}^{n}\left(T_{\text{beam}}^{i} - \overline{T}_{\text{beam}}\right)^2}$$

The minimum and maximum values of the beam transmission, $T_{\text{beam}}^{\min}$ and $T_{\text{beam}}^{\max}$ are also used below. First, let's study the dependence of the beam transmission only on a one independent parameter, while keeping other parameters at ideal nominal values.

The dependence of the beam transmission on the emittance parameter ε_x at random deviations of voltage distribution from programmed values given in the cell-table (Table 1) is presented in Figure 11. Two relative tolerance bands for the gap voltages are $\delta_U = \pm 3\%$ (Fig. 11,a) and $\delta_U = \pm 5\%$ (Fig. 11,b). The mean value of the beam transmission $\overline{T}_{\text{beam}}$ provides the transmission drop $T_{\text{beam}}^{\text{ideal}} - \overline{T}_{\text{beam}} \approx$ 2-3 % with the standard deviation $T_{\text{beam}}^{\text{st.dev}} \approx$ 3-5 % at the relative voltage tolerance $\delta_U = \pm 3\%$ and $T_{\text{beam}}^{\text{ideal}} - \overline{T}_{\text{beam}} \approx$ 3-5 % with $T_{\text{beam}}^{\text{st.dev}} \approx$ 5-8 % at $\delta_U = \pm 5\%$. The minimum values of the beam transmission, $T_{\text{beam}}^{\min}$ shows, that the beam transmission in an unlucky random experiment may drop down to $T_{\text{beam}}^{\text{ideal}} - T_{\text{beam}}^{\min} \approx$ 10-12 % at the relative voltage errors $\delta_U = \pm 3\%$ and to $T_{\text{beam}}^{\text{ideal}} - T_{\text{beam}}^{\min} \approx$ 20-25 % at $\delta_U = \pm 5\%$.

The idea of the method for treatment of the drift-tube misalignments is shown in Figure 12. The nominal drift-tube positions are shown in the Figure 12,a. The beam dynamics in the linac calculated with the cell-by-cell principle. Every cell has its own local coordinate system, $\{x_{\text{cell}}, y_{\text{cell}}, z_{\text{cell}}\}$. The fields inside the cell are described in the local coordinate system.

The random longitudinal misalignments $\delta_{z,i}$ are generated within the given tolerance band $[-\Delta_z; \Delta_z]$ and the drift tubes centers are displaced in the longitudinal direction to the new positions, $z_i + \delta_{z,i}$. If the fields are not recalculated for a new cell length, then amplitude of the field components can be corrected with the formulae $E_{z,i}^{\text{new}} = E_{z,i}^{\text{old}}\left(1-\delta_{z,i}\right)$ and $E_{r,i}^{\text{new}} = E_{r,i}^{\text{old}}\left(1-2\delta_{z,i}\right)$. For small longitudinal deviations in our IH-APF design, these corrections are about few percents.

The dependence of the beam transmission on the emittance parameter ε_x at the random longitudinal drift-tube misalignments is presented in Figure 13. Two tolerance bands are $\Delta_z = \pm 200\,\mu\text{m}$ (Fig. 13,a) and $\Delta_z = \pm 300\,\mu\text{m}$ (Fig. 13,b). The mean value of the beam transmission $\overline{T}_{\text{beam}}$ provides the transmission drop $T_{\text{beam}}^{\text{ideal}} - \overline{T}_{\text{beam}} \approx$ 1-2 % with the standard deviation $T_{\text{beam}}^{\text{st.dev}} \approx$ 3-4 % at the longitudinal drift-tube tolerance $\Delta_z = \pm 200\,\mu\text{m}$ and $T_{\text{beam}}^{\text{ideal}} - \overline{T}_{\text{beam}} \approx$ 2-3 % with $T_{\text{beam}}^{\text{st.dev}} \approx$ 5-6 % at $\Delta_z = \pm 300\,\mu\text{m}$. The minimum values of the beam transmission, $T_{\text{beam}}^{\min}$ shows, that the beam transmission in an unlucky random experiment may drop down to $T_{\text{beam}}^{\text{ideal}} - T_{\text{beam}}^{\min} \approx$ 8-12 % at the longitudinal drift-tube tolerance $\Delta_z = \pm 200\,\mu\text{m}$ and to $T_{\text{beam}}^{\text{ideal}} - T_{\text{beam}}^{\min} \approx$ 20-30 % at $\Delta_z = \pm 300\,\mu\text{m}$.

The random transverse misalignments of the drift-tubes are generated by displacements and rolling the drift-tube axes within the tolerance cylinders (see Fig.12). The length of the tolerance cylinder is equal to the length of the drift-tube and the radius is equal to the absolute value of the transverse tolerance $\left|\Delta_r\right|$. Then, the local coordinate systems of every init cells are transversely shifted and rolled in a such way, that their longitudinal axes z_{cell} passes through the points where new drift-tube axes intersects transverse planes at the gap entry and exit. In an approach, that the axially-symmetrical pattern of the gap field is preserved [18], the electrical fields are calculated first in the local coordinate system, and than transformed to the global coordinate system.

The dependence of the beam transmission on the emittance parameter ε_x at the random transversal drift-tube misalignments is presented in Figure 14. Two tolerance bands are $\Delta_r = \pm 100\,\mu\text{m}$ (Fig. 14,a) and $\Delta_r = \pm 200\,\mu\text{m}$ (Fig. 14,b). The mean value of the beam transmission $\overline{T}_{\text{beam}}$ provides the transmission drop $T_{\text{beam}}^{\text{ideal}} - \overline{T}_{\text{beam}} \leq$ 1 % with the standard deviation $T_{\text{beam}}^{\text{st.dev}} \approx$ 1-2 % at the transverse drift-tube tolerance $\Delta_r = \pm 100\,\mu\text{m}$ and $T_{\text{beam}}^{\text{ideal}} - \overline{T}_{\text{beam}} \approx$ 2-3 % with $T_{\text{beam}}^{\text{st.dev}} \approx$ 2-3 % at $\Delta_r = \pm 200\,\mu\text{m}$. The minimum values of the beam transmission, $T_{\text{beam}}^{\min}$ shows, that the beam transmission in an unlucky random experiment may drop down to $T_{\text{beam}}^{\text{ideal}} - T_{\text{beam}}^{\text{min}} \approx$ 2-4 % at the transverse drift-tube tolerance $\Delta_r = \pm 100\ \mu\text{m}$ and to $T_{\text{beam}}^{\text{ideal}} - T_{\text{beam}}^{\text{min}} \approx$ 8-15 % at $\Delta_r = \pm 200\ \mu\text{m}$.

Finally, two sets of the tolerances, containing all of the above random errors simultaneously have been calculated. Figure 15,a shows the dependence of the beam transmission for small tolerances ($\delta_U = \pm 3\%$, $\Delta_z = \pm 200\ \mu\text{m}$, $\Delta_r = \pm 100\ \mu\text{m}$) and Figure 15,b for larger tolerances ($\delta_U = \pm 5\%$, $\Delta_z = \pm 300\ \mu\text{m}$, $\Delta_r = \pm 200\ \mu\text{m}$). The mean value of the beam transmission $\overline{T}_{\text{beam}}$ provides the transmission drop $T_{\text{beam}}^{\text{ideal}} - \overline{T}_{\text{beam}} \approx$ 3-5 % with the standard deviation $T_{\text{beam}}^{\text{st.dev}} \approx$ 5-6 % at the first set of tolerances and $T_{\text{beam}}^{\text{ideal}} - \overline{T}_{\text{beam}} \approx$ 5-10 % with $T_{\text{beam}}^{\text{st.dev}} \approx$ 6-10 % at the second set of tolerances. The standard deviation values shows that the beam transmission is potentially reduced by 8-11 % at the first set of tolerances and 11-20 % at the second set of the tolerances. The minimum values of the beam transmission, $T_{\text{beam}}^{\text{min}}$ shows, that the beam transmission in an unlucky random experiment may drop down to $T_{\text{beam}}^{\text{ideal}} - T_{\text{beam}}^{\text{min}} \approx$ 10-20 % at the first set of tolerances and to $T_{\text{beam}}^{\text{ideal}} - T_{\text{beam}}^{\text{min}} \approx$ 20-40 % at the second set of the tolerances.

One may conclude, that the level of permissible errors for the drift-tube longitudinal and transversal displacements is about ±200 μ m and ±100 μ m, respectively. The fluctuations of the gap voltages should be minimized to the levels of about ±3%. At this level of tolerances the beam transmission is decreased within about 10 % (standard-deviation value) comparing to the beam transmission for the ideal structure. These tolerance levels are achievable with a modern technology, e.g. HIMAC drift-tube Alvarez linac [1] has the same tolerance band for drift-tube positions. However, it requires time-consuming procedures for a careful mechanical assembling and RF tuning.

5. Discussion

Although it is possible to construct a single research-aimed linac with the above-adopted accuracy ($\delta_U = \pm 3\%$, $\Delta_z = \pm 200\ \mu\text{m}$, $\Delta_r = \pm 100\ \mu\text{m}$), the batch-production of linacs may become hard due to a difficult and expensive alignment and tuning technology. If a developed batch-production technology is not able to provide the above accuracy, it may results in large deviations of beam parameters of every linac from average values, e.g., at tolerances $\delta_U = \pm 5\%$, $\Delta_z = \pm 300\ \mu\text{m}$, $\Delta_r = \pm 200\ \mu\text{m}$, the beam transmission of different linacs will fluctuate within $\pm(10 \div 20)$ %. Let's discuss a possible way to relax levels of permissible errors.

It is known from an analytical theory [13-15], that emittance growth due to random errors in a sequence of lenses is proportional to the number of lenses. Therefore, the beam transmission is decreased with increasing a number of drift-tubes in IH-APF linac. Also, the tuning of voltage distribution in a short IH-cavity can be done with a higher accuracy than in a long IH-cavity. The above statements mean that a possible way to relax the level of permissible errors is to shorten the IH-APF structure. It can be done by increasing transition energy between RFQ and IH-APF linacs. Let's discuss such possibility.

The present linac layout (Fig.1,b) consists of a long IH-APF structure serving as a main accelerator and a short RFQ serving as a buncher and pre-accelerator, while IH-APF uses a large RF-generator (P_{rf}=450 kW) and RFQ uses a small RF-generator (P_{rf}=125 kW). This design philosophy follows to GSI-layout [16] and is originated from the fact that a conventional RFQ has much lower shunt-impedance in comparison with IH-linac. However, GSI-linac utilizes the 7 MeV/u 4 m-long IH-linac with magnetic quadrupoles (KONUS-structure), and their design for the 7 MeV/u 4 m-long IH-APF linac has been rejected due to a high requirements for fabrication accuracy. Our 3.2m long IH-APF linac is shorter than GSI-linac, and naturally has a little bit lower requirements for fabrication accuracy. Thus, a choice of the linac layout is a trade-off between the following facts. On the one hand, the IH-APF linac has high shunt impedance, but on the other hand, it requires high fabrication accuracy.

Let's consider a possibility to increase the output energy of RFQ in order to evaluate a feasibility to shorten IH-APF structure. Following to the design procedure widely used for heavy-ion RFQ linacs, particularly for HIMAC-RFQ [1], and using GENRFQ code written by S. Yamada, the dependence of the RFQ-length, L_{RFQ} and the required RF-power, P_{RFQ} as functions of the ion energy has been calculated for a conventional 4-vane RFQ with a constant intervane voltage along the structure (Fig.16,a). In order to increase acceleration rate of RFQ, a ramped gradient-type intervane voltage can be utilized. The dependence of the RFQ-length and the required RF-power as functions of the ion energy for RFQ with a ramped gradient-voltage is also shown in Figure 16,a. In these calculations, the specific shunt impedance is assumed to be equal to $\rho = 70\ \text{k}\Omega \cdot \text{m}$ and the maximum surface field is equal to

1.8 of the Kilpatrick limit. The following definition for ρ -value has been used: $\rho = \overline{V}^2 L_{RF} / 2P_{RF}$, where $\overline{V}$ is the averaged value of intervane-voltage.

Figure 16 shows that the present 0.6Mev/u RFQ with a constant intervane-voltage should have the length L_{RFQ}=1.7 m and RF-power P_{RFQ} =70 kW (100% of Q). The extension of this constant-voltage RFQ provides the 1.3 MeV/u RFQ having the length of L_{RFQ}=3.6 m and P_{RFQ} =150 kW. The gradient-voltage RFQ with the same length L_{RFQ}=3.6 m has output energy W =1.8 MeV/u at RF-power P_{RFQ} =260 kW (100% of Q).

On the base of this 1.8 MeV/u gradient-voltage RFQ, a modified linac layout is proposed (Fig.17). It consists of the 3.8 m long RFQ (3.6 m long vanes) and a short 2 m long 34-cells IH-APF. The total length of the linac is about 6 m, and is longer on about 1 m than the length of the present linac layout (Fig.1,b). Instead of two different RF-generators with a total power P_{RFQ} =560 kW , two identical RF-generators are used with a total power P_{RFQ} =800 kW . The number of drift tubes of IH-APF is reduced to 34 instead of 68 for the present design. In spite of increasing of the linac length and total RF-power, the modified layout suggests reduced requirements for the fabrication accuracy of IH-APF linac.

Note, that acceleration rate of a gradient-voltage RFQ may be potentially improved by a factor 1.2-1.4 with usage of a modified design procedure, which is now under our development [22]. A modified 1.8 MeV/u gradient-voltage RFQ should have the length less than 3 m.

Acknowledgments

The authors would like to thank Dr. T. Murakami (NIRS), Dr. T. Mitsumoto (Sumitomo Heavy Industries) and Dr. H. Tsutsui (Sumitomo Heavy Industries) for their useful discussions.

References

[1] Y. Hirao, H. Ogawa, S. Yamada, Y. Sato, T. Yamada, K. Sato, A. Itano, M. Kanazawa, K. Noda, K. Kawachi, M. Endo, T. Kanai, T. Kohno, M. Sudou, S. Minohara, A. Kitagawa, F. Soga, E. Takada, S. Watanabe, K. Endo, M. Kumada and S. Matsumoto, "Heavy ion synchrotron for medical use — HIMAC project at NIRS-Japan", Nuclear Physics A, Vol. 538 (1992), pp. 541-550.

[2] S. Yamada, "The Progress of HIMAC and Particle Therapy Facilities in Japan", Proc. Second Asian Particle Accelerator Conf. (APAC'01), Beijing, China, 2001, pp. 829-833.

[3] K. Noda, T. Furukawa, Y. Iwata, T. Kanai, M. Komori, S. Shibuya, M. Torikoshi, S. Yamada, "HIMAC and New Facility Design for Wide Spread Use of Carbon Cancer Therapy", to be published in Proc. of the 3rd Asian Particle Accelerator conference (APAC-2004), Gyeongju, Korea, March 22-26, 2004.

[4] V. Kapin, S. Yamada; Y. Iwata, "Design of APhF-IH Linac for a Compact Medical Accelerator", report HIMAC-075, December 2003 by NIRS. (full-text PDF-file at HEPDOC: http://weblib.cern.ch/share/hepdoc/).

[5] Y. Iwata, S. Yamada, and V. Kapin, "Beam dynamics of alternating-phase-focused linac", report HIMAC-079, February 2003 by NIRS. (full-text PDF-file at HEPDOC: http://weblib.cern.ch/share/hepdoc/).

[6] Y. Iwata, T. Furukawa, T. Kanai, M. Komori, K. Noda, S. Shibuya, M. Torikoshi, S. Yamada, V. Kapin, "Beam dynamics of alternating-phase-focused linac for medical accelerators", to be published in Proc. of the 3rd Asian Particle Accelerator conference (APAC-2004), Gyeongju, Korea, March 22-26, 2004.

[7] S. Yamada, T. Hattori, A. Itano, M. Kanazawa, A. Kitagawa, T. Kohno, Y. Miyazawa, O. Morishita, K. Noda, H. Ogawa, K. Sato, Y. Sato, K. Sawada, M. Sudou, E. Takada, T. Yamada and Y. Hirao, "Injector System of HIMAC", Proc. of the 1990 Linear Accelerator Conference, 1990 by LANL, pp. 593-595.

[8] Y. Iwata, T. Furukawa, T. Kanai, N Kanematsu, Y. Kobayashi, M. Komori, S. Minohara, K. Noda, S. Shibuya, M. Torikoshi, S. Yamada, K. Yusa, V. Kapin, "Alternating-Phase-Focused linac for an injector of medical synchrotrons", to be presented at The 9th European Particle Accelerator Conference (EPAC'04), 5-9 July, 2004 Lucerne.

[9] "CST MICROWAVE STUDIO", WWW: http://www.cst-world.com.

[10] E. Nolte, R. Geier, W. Schollmeier and S. Gustavsson, “Improved Performance of the Munich Heavy Ion Postaccelerator”, Nucl. Instrum. & Methods, Vol. 201 (1982), pp. 281-285.

[11] S. Yamada, T. Hattori, T. Fujino, T. Fukushima, T. Murakami, E. Tojyo, and K.Yoshida, “IH Linac Development at INS”, report INS-NUMA-57, 1985 by Institute for Nuclear Study, Tokyo Univ.

[12] U. Ratzinger, “Interdigital RF structures”, Proc. 1990 Linear Accelerator Conference, Los Alamos, report LA-2004-C, 1991, pp.525-529.

[13] L. Smith and R.L. Gluckstern, “Focusing in Linear Ion Accelerators”, The Review of Scientific Instrum., Vol. 26, No. 2, 1955, pp. 220-228.

[14] I.M. Kapchinskiy, “Theory of Resonance Linear Accelerators”, Harwood Academic Publishers, Amsterdam, 1985.

[15] T.P. Wangler, “Principles of RF Linear Accelerators”, 1998, J. Wiley & Sons, Inc.

[16] S. Minaev, U. Ratzinger, B. Schlitt , “APF or KONUS drift tube structures for medical synchrotron injectors – a comparison”, Proceedings of the 1999 Particle Accelerator Conference, New York, 1999, pp.3555-3557.

[17] V.K. Baev, “Effects of errors on the Particles Dynamics in Accelerator with Focusing by an Axial-Symmetrical Accelerating Field”, *In collected papers of Moscow Engineering Physics Institute*: “Accelerator-Based Radiative-Acceleration Complexes”, Moscow, Energoatomizdat, 1983, pp. 39-42 (in Russian).

[18] A.N. Antropov, N.M. Gavrilov, S.A. Minaev, “The tolerances for accelerating structure parameters of the ion linac with increased particle capture”, *In collected papers of Moscow Engineering Physics Institute:* “Linac Systems and applications of the charged particle beams”, Moscow, Energoatomizdat, 1987, pp.30-35 (in Russian)

[19] J.H. Billen and L.M. Young, “Poisson/Superfish” LA-UR-96-1834, 2002.

[20] V.V. Rassadin, “Mathematical Simulation of Electrical Fields and Beam Dynamics in the Low-Energy Ion Linacs with Focusing by Axial-Symmetrical Accelerating Fields”, Dissertation for Candidate Degree, MEPhI, Moscow, 1991 (in Russian).

[21] Y.K. Batygin, “Particle-in Cell Code BEAMPASS for Beam Dynamics Simulations with Space Charge”, report RIKEN-AF-AC-17, 2000 by Inst. Phys. & Chem. Res. (RIKEN).

[22] V.Kapin and S.Yamada, “RFQ with an Increased Energy Gain”, to be presented at XIX Russian Conf. On Charged Particle Accelerators (RUPAC-2004), Oct.4-9, Dubna, Russia. (http://www.jinr.ru/RuPAC2004/)

Table 1. The cell table of the IH-APF linac

Cell No.	L, mm	L_1, mm	L_g, mm	L_2, mm	U_g^0, MV	ϕ_s, deg
1	58.978	40.00	9.80	9.18	0.0800	-90.000
2	89.364	9.08	10.00	11.31	0.1610	-81.573
3	123.599	11.21	10.20	12.83	0.1640	-44.585
4	159.723	12.63	10.60	12.90	0.1690	7.735
5	194.852	12.70	11.00	11.43	0.1740	55.402
6	226.473	11.33	11.20	9.09	0.1770	82.939
7	253.598	8.99	11.40	6.74	0.1790	81.933
8	277.225	6.64	11.60	5.39	0.1820	52.552
9	299.884	5.19	12.00	5.47	0.1870	5.682
10	324.364	5.17	12.60	6.71	0.1920	-41.371
11	352.636	6.61	12.80	8.86	0.1960	-73.631
12	385.607	8.76	13.00	11.21	0.1990	-81.984
13	423.143	11.01	13.40	13.13	0.2010	-63.934
14	464.013	12.93	13.80	14.14	0.2060	-25.559
15	506.000	13.94	14.20	13.84	0.2120	19.622
16	546.510	13.54	14.80	12.17	0.2170	57.215
17	583.538	12.07	15.00	9.96	0.2210	77.036
18	616.437	9.76	15.40	7.74	0.2240	73.968
19	646.183	7.54	15.80	6.41	0.2280	49.011
20	674.988	6.11	16.40	6.30	0.2330	10.228
21	705.318	6.10	16.80	7.43	0.2380	-30.086
22	738.999	7.33	17.00	9.35	0.2410	-60.731
23	776.991	9.25	17.20	11.54	0.2420	-74.528
24	819.451	11.44	17.40	13.62	0.2440	-68.468
25	865.742	13.52	17.60	15.17	0.2460	-44.477
26	914.443	14.97	18.00	15.73	0.2500	-9.609
27	963.586	15.53	18.40	15.22	0.2540	26.393
28	1011.178	15.02	18.80	13.78	0.2570	54.827
29	1055.786	13.68	19.00	11.93	0.2590	69.817
30	1096.943	11.83	19.20	10.13	0.2600	68.517
31	1135.288	10.03	19.40	8.92	0.2620	51.538
32	1172.353	8.82	19.60	8.65	0.2660	23.268
33	1210.014	8.35	20.20	9.11	0.2690	-9.228
34	1249.880	8.91	20.60	10.35	0.2730	-38.649
35	1293.020	10.25	20.80	12.09	0.2750	-59.335
36	1339.973	11.99	21.00	13.97	0.2770	-67.751
37	1390.787	13.87	21.20	15.75	0.2780	-62.619
38	1445.014	15.65	21.40	17.18	0.2800	-45.241
39	1501.809	16.98	21.80	18.01	0.2940	-19.486
40	1559.846	17.81	22.20	18.02	0.2980	9.663
41	1617.534	17.82	22.60	17.26	0.3010	36.053
42	1673.513	17.06	23.00	15.91	0.3040	55.163
43	1726.911	15.81	23.20	14.38	0.3060	64.069
44	1777.532	14.28	23.40	12.94	0.3080	61.552
45	1825.904	12.84	23.60	11.93	0.3100	48.308

Cell No.	L, mm	L_1, mm	L_g, mm	L_2, mm	U_g^0, MV	ϕ_s, deg
46	1873.138	11.73	24.00	11.50	0.3130	26.994
47	1920.615	11.30	24.40	11.78	0.3170	1.697
48	1969.621	11.58	24.80	12.63	0.3200	-23.120
49	2021.127	12.43	25.20	13.88	0.3230	-43.594
50	2075.746	13.78	25.40	15.44	0.3250	-56.901
51	2133.762	15.24	25.80	16.97	0.3270	-61.368
52	2195.153	16.87	26.00	18.52	0.3290	-56.569
53	2259.582	18.42	26.20	19.81	0.3310	-43.441
54	2326.406	19.61	26.60	20.61	0.3340	-24.218
55	2394.724	20.41	27.00	20.91	0.3370	-2.009
56	2463.492	20.71	27.40	20.66	0.3400	19.872
57	2531.679	20.46	27.80	19.93	0.3420	38.512
58	2598.435	19.83	28.00	18.93	0.3450	51.691
59	2663.227	18.83	28.20	17.76	0.3460	57.976
60	2725.924	17.56	28.60	16.53	0.3480	56.778
61	2786.818	16.43	28.80	15.66	0.3500	48.425
62	2846.566	15.56	29.00	15.19	0.3520	34.168
63	2906.057	14.99	29.40	15.10	0.3540	16.016
64	2966.225	14.90	29.80	15.47	0.3570	-3.621
65	3027.891	15.27	30.20	16.20	0.3590	-22.350
66	3091.683	16.00	30.60	17.19	0.3620	-38.119
67	3158.023	16.99	31.00	18.35	0.3630	-49.359
68	3237.470	18.25	31.20	30.00	0.3650	-55.044

Table 2. The parameters calculated with MWS-code.

	Parameter	Units	The calculation details
1	The resonance frequency, f_0	MHz	(in GHz) directly by MWS
2	Q-factor, Q_0	-	directly by MWS using "Loss and Q calculation"
3	The power due to surface losses, $W_{\text{loss}}^{\text{peak}}$	kW	(in W) directly by MWS using "Loss and Q calculation"
4	The RF power dissipation (RMS-value), $P_{\text{RF}}^{\text{rms}}$	kW	a) $P_{\text{RF}}^{\text{rms}} = 2\pi f_0 \cdot W / Q_0$, where W is the total energy (1 Joule); b) $P_{\text{RF}}^{\text{rms}} = W_{\text{loss}}^{\text{peak}} / 2$
5	The gap voltage along the cell axis, $V_{\text{g}} = \int_0^{L_{\text{cell}}} E_z(0,0,z) \cdot dz$	kV	(in V) directly by MWS using the template based post - processing "OD Results => OD value from 3D field on curve: Integral of z-component"
6	"The vertical gap voltage" (The integral of the y-component of the E-field along the cell axis), $V_{\text{y}} = \int_0^{L_{\text{cell}}} E_y(0,0,z) \cdot dz$	kV	(in V) directly by MWS using the template based post- processing "OD Results => OD value from 3D field on curve: Integral of y-component"
7	Ratio V_y / V_{g}	%	Calculation using results of lines 5 and 6.
8	Radio-technical shunt impedance, R_{sh}	kΩ	Calculations with formula $R_{\text{sh}} = V_{\text{g}}^2 / 2P_{\text{RF}}^{\text{rms}}$ using results of lines 4 and 5.
9	"E-Maximum-2D [V/m]", $E_{\text{max}}^{\text{MWS,2D}}$ "H-Maximum-2D [kA/m]", $H_{\text{max}}^{\text{MWS,2D}}$ " I-Maximum-3D [kA/m]", $I_{\text{max}}^{\text{MWS,3D}}$	V/m; kA/m; kA/m	The values shown by MWS on the field pictures
10	Ratio between surface and the gap voltage, $E_{\text{s}} / E_{\text{g}} \equiv E_{\text{s}} l_{\text{g}} / V_{\text{g}}$	-	Calculations with formulae $E_{\text{max}}^{\text{MWS,2D}} \cdot l_{\text{g}} / V_{\text{g}}$ using the above values at line 5 and 9
11	"MeshCells" – number		MWS mesh generator

Table 3. The basic geometrical parameters of the IH-cavities

Parameter, mm		"6-gap L22"	"21-gap L22"	"6-gap L44"	"21-gap L44"	"6-gap L66"
The cell length	L_{cell}	22	22	44	44	66
IH-tank: Length, Radius	L_{tank} , R_{tank}	168, 180	498,150	296,180	956, (170-190)	396,180
Rectangular Ridges						
Total sizes: LxHxW	$H_{\text{R}}, L_{\text{R}}, W_{\text{R}}$	130x128x 40	130x458x 40	130x256x 40	150x916x 40	130x356x 40
Distance from the ridge top to the tank axis	a_{R}	50	50	50	50	50
Distance to the tank bottoms	l_{R}	20	20	20	20	20
Internal drift-tubes:						
The length	L_{DT}	12	12	24	24	36
The outer radius	r_{DT}	14	14	14	14	15
The aperture radius	a_{DT}	7	7	7	14	7
The chamfer radii: internal/ outer	$r_{\text{int}} / r_{\text{out}}$	2/4.5	2/4.5	2/4.5	2/4.5	2/5.5
The gap length	L_{g}	10	10	20	20	30
Flange drift-tubes:						
The length	$l_{\text{flange,DT}}$	24	24	28	28	18
Cylindrical Stem:						
The radius	-	-	4.5	4.5	4.5	4.5
Conical Stem:						
The radii: at top/bottom	3/10	3/10	-	-		-

Table 4. The calculated parameters of IH-cavities versus the ridge angle α_R.

Parameter	"6-gap-L22" (L_{cell} =22mm)					"21-gap L22" (L_{cell} =22mm)				
Angle, α_R, deg	0	10	20	30	40	0	10	20	30	40
f_0, MHz	269	287	300	312	322	189	195	200	206	211
Solver time (one iteration), min.	100	95	100	101	90	62	52	45	49	51
Mesh-Cells, millions	0.9	1.0	1.0	1.0	1.1	0.9	0.86	0.9	0.9	0.9
Q_0	6015	6213	6372	6504	6614	9013	9272	9501	9730	9933
W_{loss}^{peak}, kW	561	580	592	603	612	264	264	265	265	267
P_{RF}^{rms}, kW	281	290	296	301	306	132	132	132	133	134
R_{sh}, kΩ	442	446	450	453	454	315	322	328	331	333
V_g, kV	498	508	516	522	527	288	292	294	296	298
V_y, kV	10.1	10.3	10.4	10.5	10.5	5.3	5.4	5.4	5.5	5.5
V_y/V_g,%	2.0	2.0	2.0	2.0	2.0	1.8	1.8	1.8	1.9	1.9
$E_{max}^{MWS,2D}$, V/m	1.06 E8	1.08 E8	1.11 E8	1.12 E8	1.13 E8	5.6 E7	5.7 E7	5.7 E7	5.8 E7	5.8 E7
$H_{max}^{MWS,2D}$, kA/m	236	255	271	283	295	50.1	51.6	52.7	53.8	54.7
$E_{max}^{MWS,2D}/E_g$	2.13	2.15	2.15	2.14	2.14	1.94	1.95	1.94	1.96	1.95

Table 4. (continued)

Parameter	"6-gap L44" (L_{cell} =44mm)					"6-gap L66" (L_{cell} =66mm)				
Angle, α_R, deg	0	10	20	30	40	0	10	20	30	40
f_0, MHz	268	281	291	301	309	258	269	278	286	294
Solver time (one iteration), min.	130	183	141	160	160	210	230	210	220	230
Mesh-Cells, millions	1.4	1.5	1.5	1.5	1.6	1.8	1.9	1.9	2.0	2.1
Q_0	8649	8893	9243	9576	9878	8927	9112	9375	9621	9827
W_{loss}^{peak}, kW	389	397	396	395	393	363	371	372	374	376
P_{RF}^{rms}, kW	195	199	198	197	197	182	185	186	187	188
R_{sh}, kΩ	922	944	975	1000	1019	905	924	946	962	969
V_g, kV	599	612	622	628	633	573	566	594	600	604
V_y, kV	35.4	36.0	36.6	37.0	37.3	62.5	63.7	64.6	65.2	65.7
V_y/V_g,%	5.9	5.9	5.9	5.9	5.9	10.9	10.9	10.9	10.9	10.9
$E_{max}^{MWS,2D}$, V/m	8.7 E7	8.9 E7	9.0 E7	9.1 E7	9.2 E7	7.1 E7	7.2 E7	7.3 E7	7.4 E7	7.5 E7
$H_{max}^{MWS,2D}$, kA/m	83.7	89.4	93.7	97.1	100	77.3	82.1	85.5	88.4	90.8
$E_{max}^{MWS,2D}/E_g$	2.9	2.9	2.9	2.9	2.9	3.7	3.8	3.7	3.7	3.7

Table 5.

The calculated parameters of three 21-gap L_{cell} =44 mm IH-cavities having different tank radii (170 mm, 180mm, and 190 mm) versus the ridge angle.

Parameter	The tank radius R_{tank} = 170 mm								
Angle, α_R, deg	0	5	10	15	20	25	30	35	40
f_0, MHz	**200**	**203**	**206**	209	211	214	218	221	224
Solver time (one iteration), min.	60	120	85	108	92	108	84	114	94
Mesh-Cells, millions	0.9	1.3	1.0	1.3	1.1	1.3	1.1	1.3	1.2
Q_0	13081	13195	13333	12980	12899	13109	13266	13266	13343
W_{loss}^{peak}, kW	192	193	194	201	205	205	206	206	208
P_{RF}^{rms}, kW	96	96	97	101	103	103	103	103	104
R_{sh}, kΩ	**648**	**651**	**655**	**627**	**608**	**602**	**603**	**603**	**599**
V_g, kV	352.7	354.4	356.2	355.6	353.6	351.2	352.6	353.0	359.0
V_y, kV	20.5	20.6	20.9	21.0	21.0	21.0	21.2	21.3	21.5
V_y/V_g, %	0.058	0.058	0.059	0.059	0.059	0.060	0.060	0.060	0.060
$E_{max}^{MWS,2D}$, V/m	4.21 E7	4.22 E7	4.25 E7	4.26 E7	4.25 E7	4.24 E7	4.27 E7	4.27 E7	4.26 E7
$H_{max}^{MWS,2D}$, kA/m	24.7	25.1	25.4	25.7	25.9	26.1	26.3	26.6	26.1
$I_{s,max}^{MWS,3D}$, kA/m	**38.6**	**38.2**	**37.8**	**37.6**	**37.4**	**37.3**	**37.1**	**37.2**	**33.0**
$E_{max}^{MWS,2D}/E_g$	**2.4**	**2.4**	**2.4**	**2.4**	**2.4**	**2.4**	**2.4**	**2.4**	**2.4**

Table 5. (continued)

Parameter	The tank radius R_{tank} = 180 mm								
Angle, α_R, deg	0	5	10	15	20	25	30	35	40
f_0, MHz	**190**	**193**	**195**	**198**	**201**	**204**	**207**	**211**	**214**
Solver time (one iteration), min.	80	53	107	153	117	128	120	130	9h
Mesh-Cells, millions	1.1	1.4	1.1	1.3	1.3	1.4	1.2	1.4	1.4
Q_0	13145	13271	13436	13070	13007	13198	13406	13530	13980
W_{loss}^{peak}, kW	181	182	183	190	194	194	194	196	192
P_{RF}^{rms}, kW	91	91	91	95	97	97	97	98	96
R_{sh}, kΩ	**668**	**672**	**677**	**648**	**630**	**621**	**625**	**623**	**656**
V_g, kV	347.9	349.7	351.8	351.2	349.5	347.0	348.3	349.1	354.9
V_y, kV	20.2	20.4	20. 8	20.8	20.9	20.8	21.1	21.4	21.4
V_y/V_g, %	0.058	0.058	0.059	0.059	0.060	0.060	0.061	0.061	0.060
$E_{max}^{MWS,2D}$, V/m	4.15 E7	4.17 E7	4.20 E7	4.21 E7	4.21 E7	4.20 E7	4.23 E7	4.26 E7	4.22 E7
$H_{max}^{MWS,2D}$, kA/m	23.8	24.1	24.4	24.6	24.9	25.1	25.3	25.5	25.1
$I_{s,max}^{MWS,3D}$, kA/m	**36.1**	**35.8**	**35.5**	**35.3**	**35.2**	**35.1**	**35.0**	**35.0**	31.5
$E_{max}^{MWS,2D}/E_g$	**2.4**	**2.4**	**2.4**	**2.4**	**2.4**	**2.4**	**2.4**	**2.4**	**2.4**

Table 5. (continued)

Parameter	The tank radius R_{tank} = 190 mm								
Angle, α_R, deg	0	5	10	15	20	25	30	35	40
f_0, MHz	**180**	**183**	**186**	**189**	**192**	**194**	**198**	**201**	**204**
Solver time (one iteration), min.	110	97	120	115	124	123	116	126	141
Mesh-Cells, millions	1.2	1.2	1.3	1.4	1.4	1.4	1.4	1.4	1.5
Q_0	13144	13271	13456	13073	12975	13241	13483	13621	14130
$W_{\text{loss}}^{\text{peak}}$, kW	172	173	174	182	186	185	185	186	182
$P_{\text{RF}}^{\text{rms}}$, kW	86	87	87	91	93	92	92	93	91
R_{sh}, kΩ	**684**	**688**	**696**	**664**	**633**	**638**	**643**	**642**	**677**
V_{g}, kV	343.4	345.2	347.9	347.2	342.9	343.2	344.4	345.2	350.8
V_{y}, kV	20.1	20.3	20.6	20.7	/20.7	20.7	21.0	21.3	21.3
V_y/V_{g},%	0.059	0.059	0.059	0.059	0.060	0.060	0.060	0.062	0.06
$E_{\max}^{\text{MWS,2D}}$, V/m	4.11 E7	4.12 E7	4.16 E7	4.17 E7	4.16 E7	4.20 E7	4.19 E7	4.22 E7	4.18 E7
$H_{\max}^{\text{MWS,2D}}$, kA/m	23.0	23.4	23.7	23.9	24.1	24.3	24.4	24.6	24.2
$I_{\text{s,max}}^{\text{MWS,3D}}$, kA/m	**34.0**	**33.7**	**33.4**	**33.3**	**33.1**	**33.2**	**33.1**	**33.1**	**30.4**
$E_{\max}^{\text{MWS,2D}}/E_{\text{g}}$	**2.4**	**2.4**	**2.4**	**2.4**	**2.4**	**2.4**	**2.4**	**2.4**	**2.4**

Table 6. The calculated parameters of the 6-gap and 21-gap IH-cavities having the same cell length L_{cell} =22 mm and different sizes of conical and triangular stems.

Parameter	"6-gap-L22" (L_{cell} =22mm)					"21-gap L22" (L_{cell} =22mm)				
Stem type & sizes	conical stem d_1=3.0, d_2=20	triangular stem (thickness 10mm) h_{hor}=40mm, h_{vert}=40mm, s_{vert}=3.0mm, s_{hor}=5mm				conical stem d_1=3.0, d_2=20	triangular stem (thickness 10mm) h_{hor}=40mm, h_{vert}=40mm, s_{vert}=3.0mm, s_{hor}=5mm			
Distance, ξ_s , mm	-	0	5	10	15	0	0	5	10	15
f_0 , MHz	269	265	268	268	268	*189*	*189*	*191*	*192*	*191*
Solver time (one iteration), min.	100	134	143	146	134	*62*	*192*	*180*	*130*	*190*
Mesh-Cells, millions	0.9	1.2	1.4	1.3	1.1	*0.9*	*1.3*	*1.2*	*1.6*	*1.3*
Q_0	6015	5935	6046	6043	6074	*9013*	*7964*	*8839*	*9076*	*8734*
$W_{\text{loss}}^{\text{peak}}$, kW	561	562	558	558	554	*264*	*299*	*271*	*165*	*275*
$P_{\text{RF}}^{\text{rms}}$, kW	281	281	279	279	277	*132*	*149*	*136*	*133*	*137*
R_{sh} , kΩ	442	461	477	460	451	*315*	*312*	*329*	*350*	*315*
V_{g} , kV	498	509	516	506	500	*288*	*305*	*299*	*305*	*294*
V_{y} , kV	10.1	7.2	9.2	9.8	11.0	*5.3*	*5.1*	*5.8*	*7.2*	*7.3*
V_y / V_{g} , %	2.0	1.4	1.8	1.9	2.2	*1.8*	*1.7*	*1.9*	*2.4*	*2.5*
$E_{\max}^{\text{MWS,2D}}$, V/m	1.06 E8	1.1 E8	1.1 E8	1.1 E8	1.1 E8	*5.6 E7*	*6.2 E7*	*5.9 E7*	*6.5 E7*	*6.0 E7*
$H_{\max}^{\text{MWS,2D}}$, kA/m	236	68	65	68	70	*50.1*	*32.8*	*33.3*	*33.5*	*40.8*
$E_{\max}^{\text{MWS,2D}} / E_{\text{g}}$	2.1	2.2	2.1	2.2	2.2	*1.9*	*2.0*	*2.0*	*2.1*	*2.0*
$I_{\text{s,max}}^{\text{MWS,3D}}$, kA/m	**278**	**148**	**139**	**151**	**132**	*62*	*66*	*66*	*70*	*69*

Table 7. The parameters of the 6-gap cavity with cell length L_{cell} =44 mm at different sizes of the cylindrical and triangular stems.

Parameter	"6-gap L44" (L_{cell} =44mm)							
Stem type & sizes	cylndrical stem d_c=9.0	triangular stem (thickness 10mm) h_{hor}=40mm, h_{vert}=40mm, s_{vert}=9.0mm, s_{hor}=5mm				triangular stem (thickness 10mm) h_{hor}=80mm, h_{vert} =40mm, s_{vert}=9mm, s_{hor}=5mm		
Distance, ξ_s , mm	-	0	5	10	15	0	10	20
f_0 , MHz	268	269	270	271	271	269	270	270
Solver time (one iteration), min.	130	106	144	180	102	103	161	140
Mesh-Cells, millions	1.4	1.5	1.7	1.8	1.5	1.4	1.7	1.7
Q_0	8649	8116	8328	8341	8338	7515	8206	6867
W_{loss}^{peak} , kW	389	416	408	408	409	449	414	495
P_{RF}^{rms} , kW	195	208	204	204	204	225	207	247
R_{sh} , kΩ	922	853	855	837	826	781	803	648
V_g , kV	599	596	590	584	581	592	577	566
V_y , kV	35	37	38	39	43	37	40	47
V_y/V_g , %	5.9	6.1	6.4	6.7	6.7	6.2	7.0	8.3
$E_{max}^{MWS,2D}$, V/m	8.7 E7	6.9 E7	6.9 E7	6.7 E7	6.3 E7	6.9 E7	6.9 E7	8.0 E7
$H_{max}^{MWS,2D}$, kA/m	83.7	60.7	59.5	57.1	61.1	62.1	58.7	69.1
$E_{max}^{MWS,2D}/E_g$	2.9	2.3	2.3	2.3	2.5	2.3	2.4	2.8
$I_{s,max}^{MWS,3D}$, kA/m	85	76	111	92	89	82	100	95

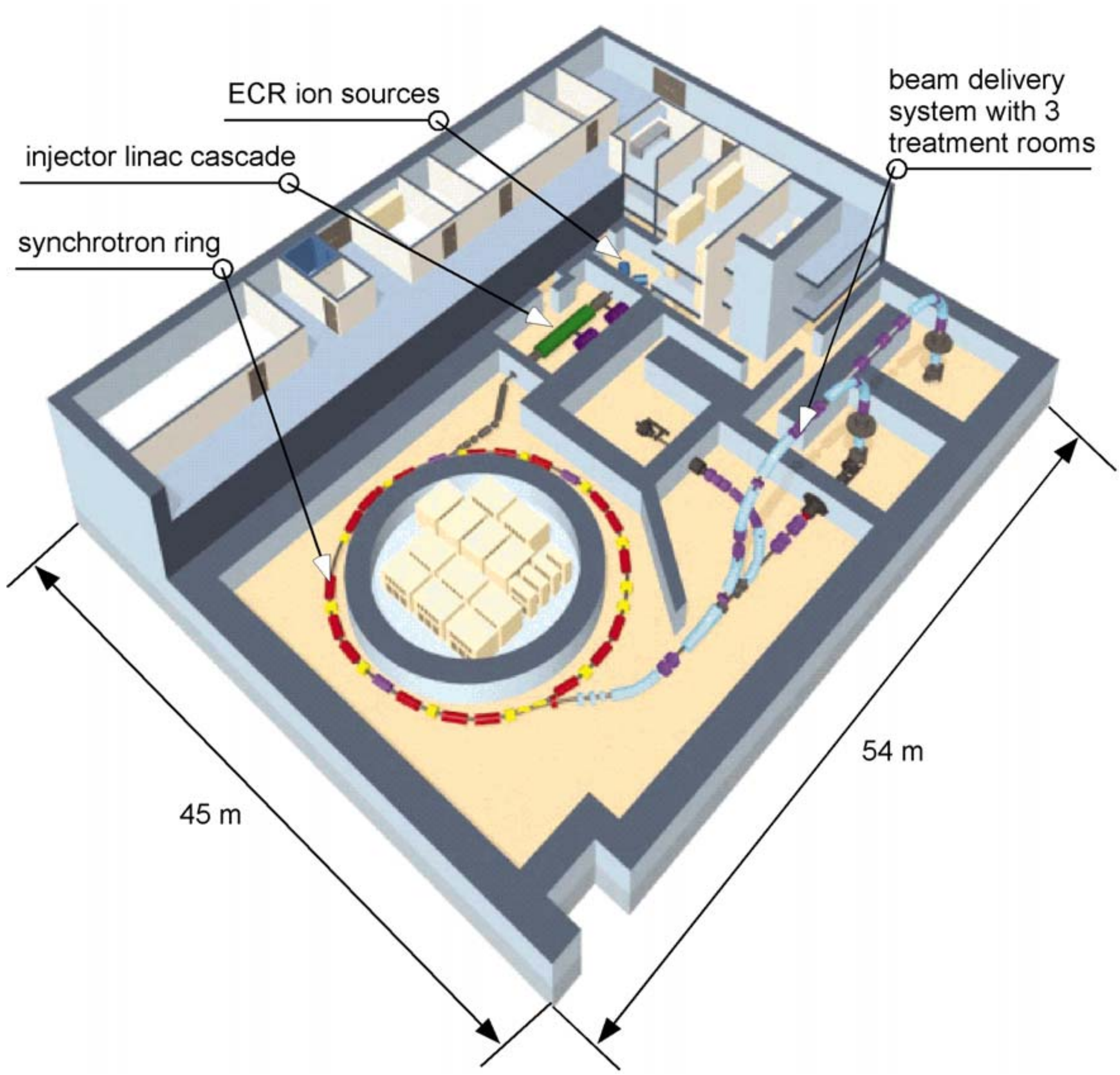

a)

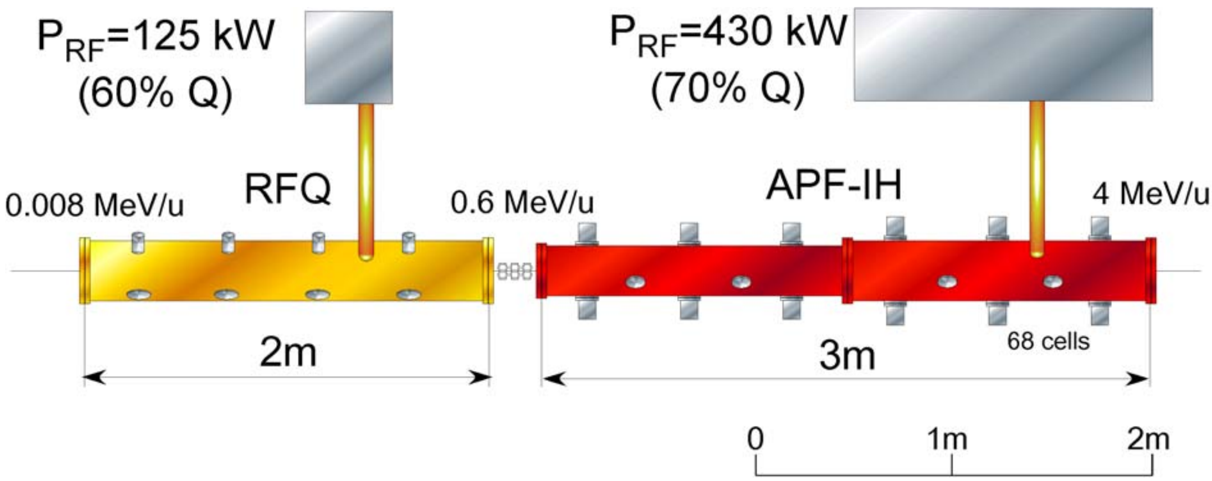

b)

Fig. 1. The accelerator complex for compact medical facility:
the general view (a) and the injector linac (b).

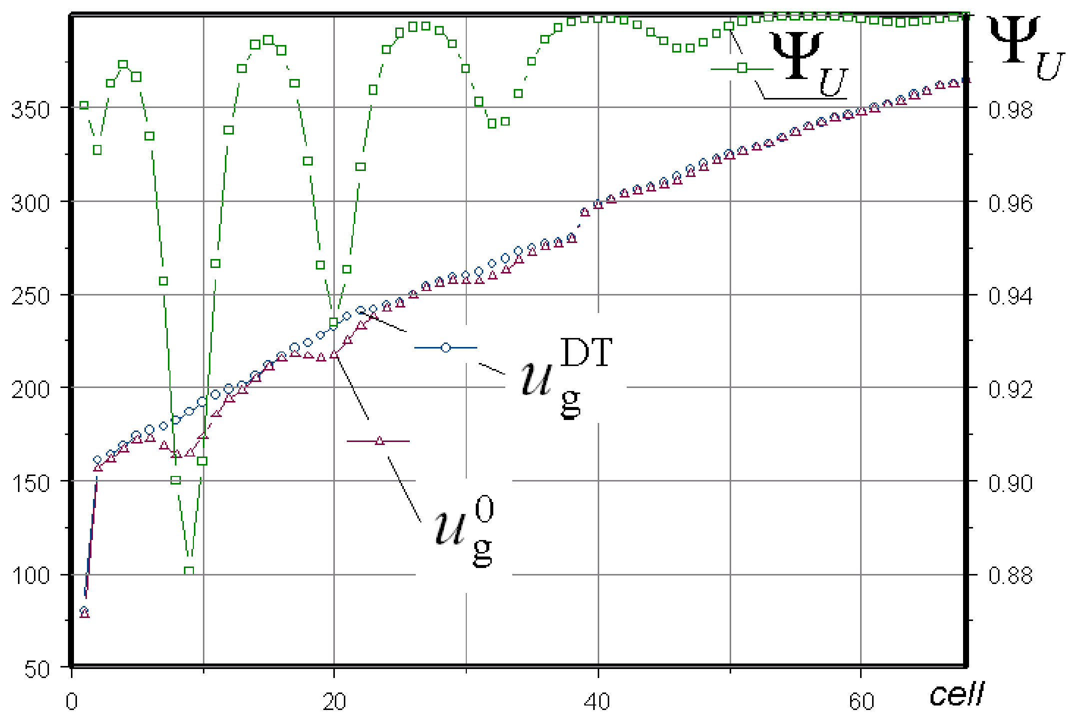

a)

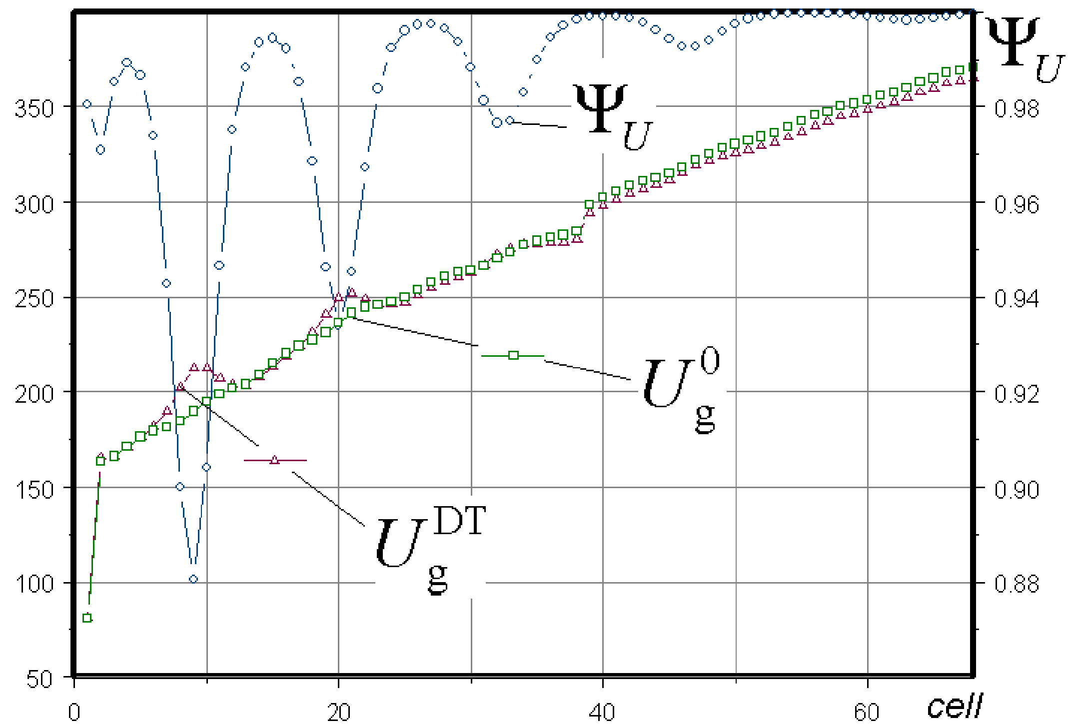

b)

Fig. 2. The voltage re-calculation procedure:

a) the voltages u_g^{DT} and u_g^0, and the factor Ψ_U as functions of the cell number;

b) the restored voltage U_g^{DT} and U_g^0, and the factor Ψ_U versus the cell number.

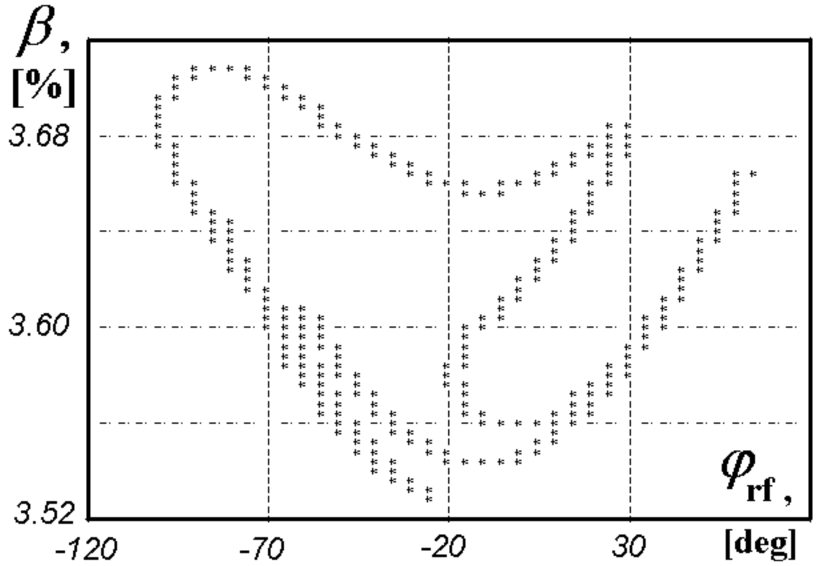

a)

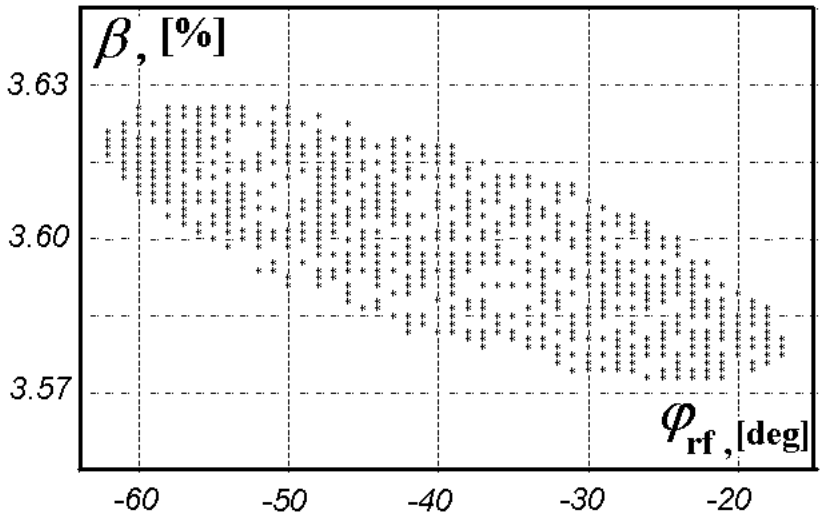

b)

Fig. 3. The longitudinal phase space:

a) The longitudinal acceptance of the IH-APF linac calculated for axial particles;

b) The longitudinal emittance of the injected particles.

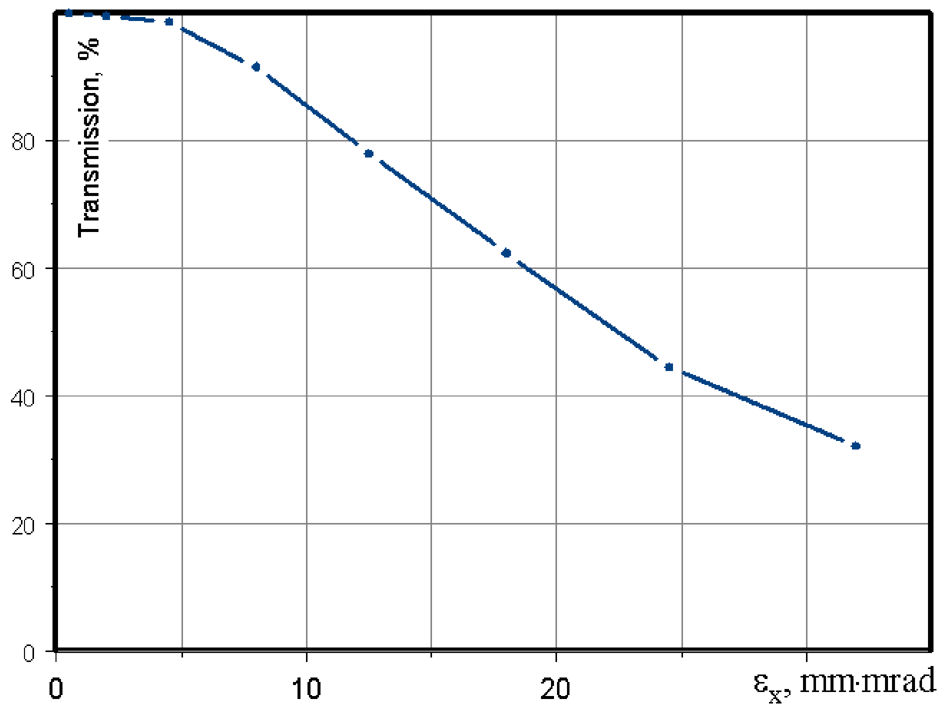

a)

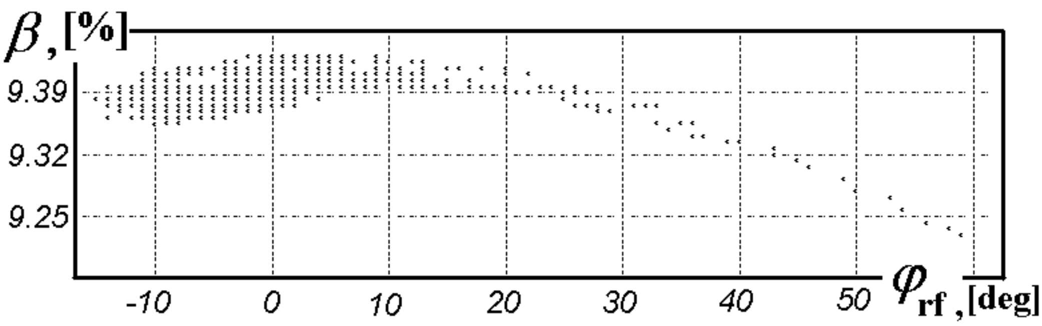

b)

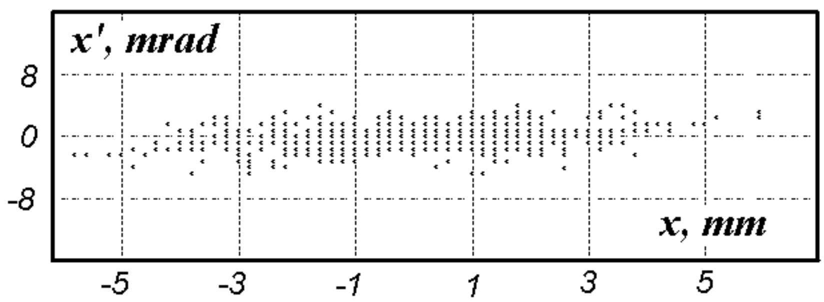

c)

Fig. 4. The results of the beam dynamics simulations:

a) The beam transmission T_{beam} as function of the emittance parameter ε_x;

b) The longitudinal beam emittance at the exit (ε_x=8.0 mm$\times$mrad);

c) The transverse beam emittance at the exit (ε_x=8.0 mm$\times$mrad).

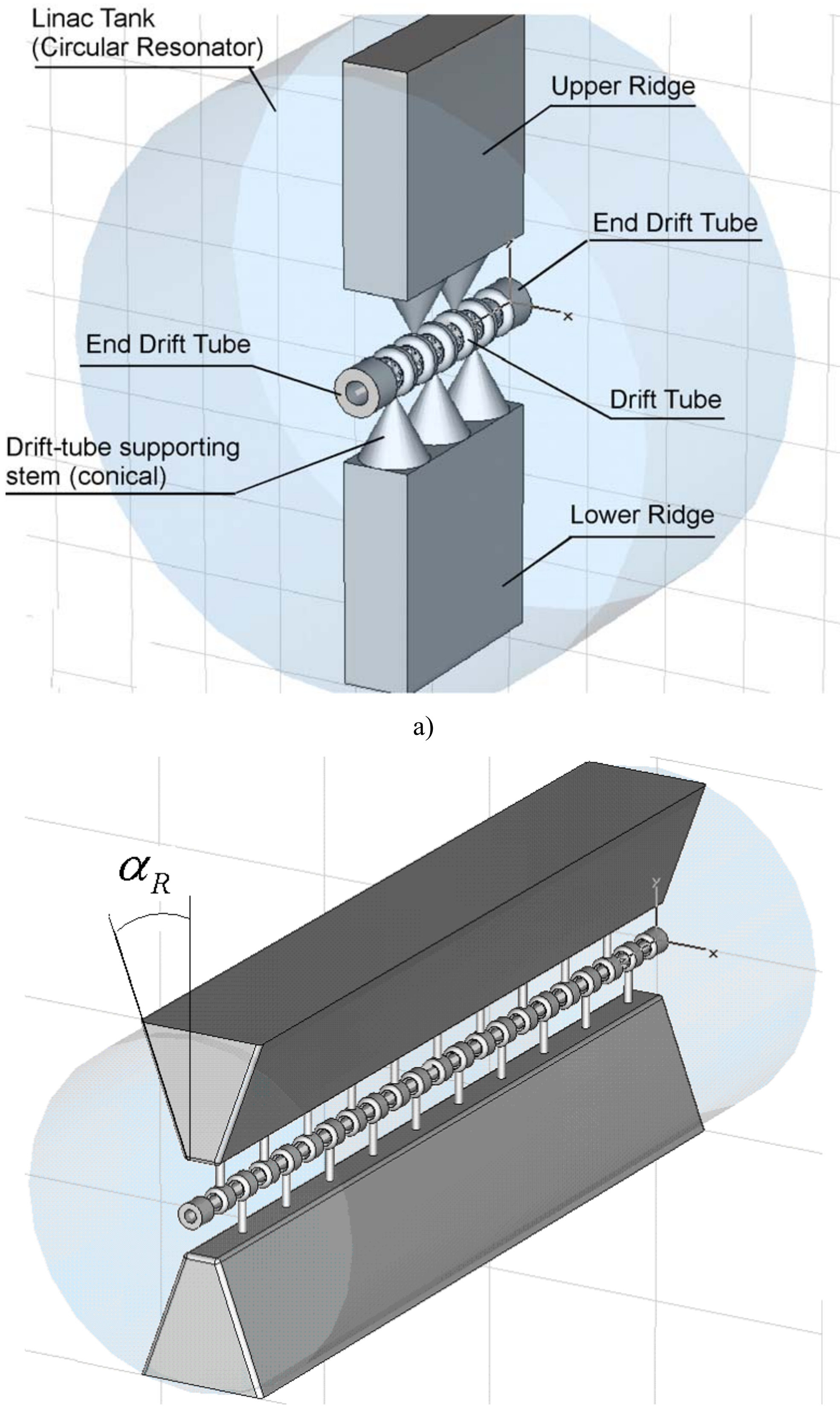

Fig. 5. The schematic drawing of an IH-cavity (a) and
the 21-gap IH-cavity with trapezoidal ridge (b)

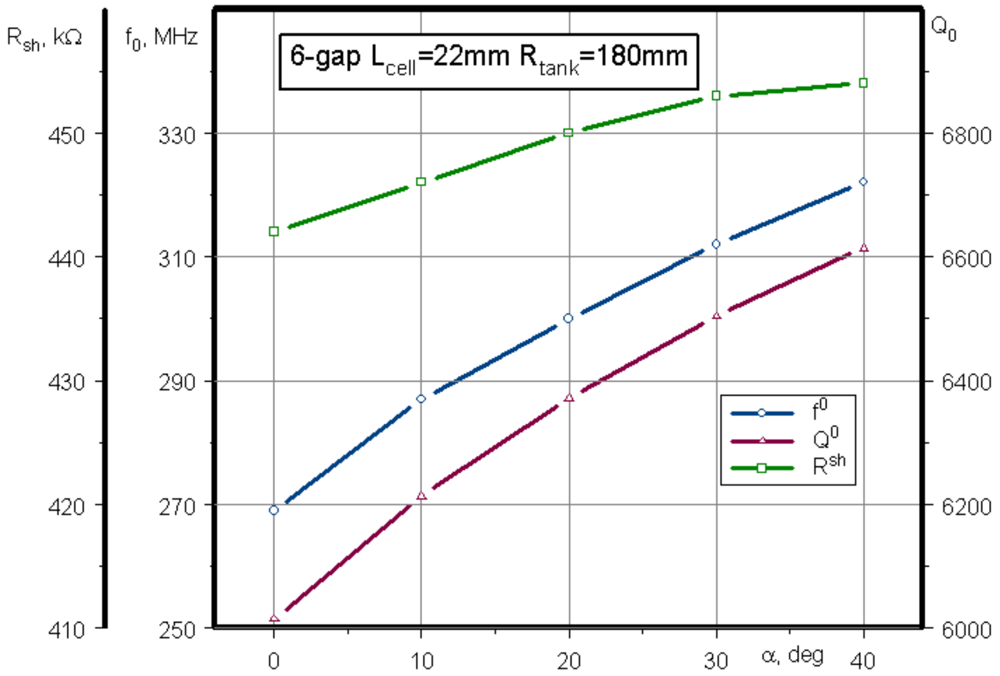

a)

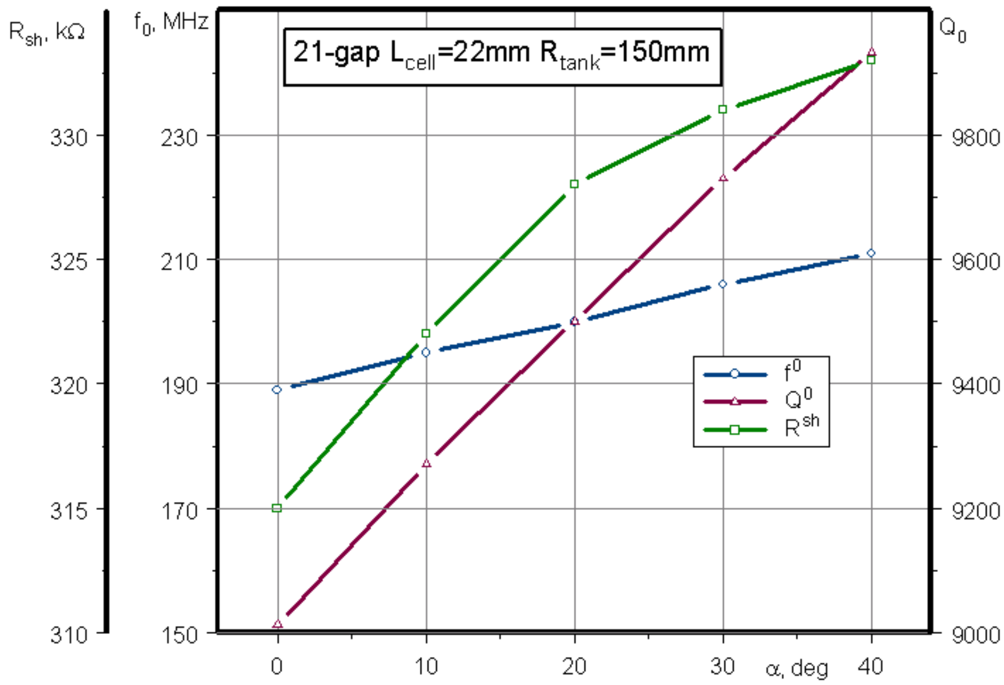

b)

Fig. 6. The calculated values of Q_0, frequency f_0, and R_{sh} versus the ridge angle α_R for IH-cavities with L_{cell} =22 mm:

a) The 6-gap cavity with the tank radius R_{tank} =180 mm;

b) The 21-gap cavity with the tank radius R_{tank} =150 mm;

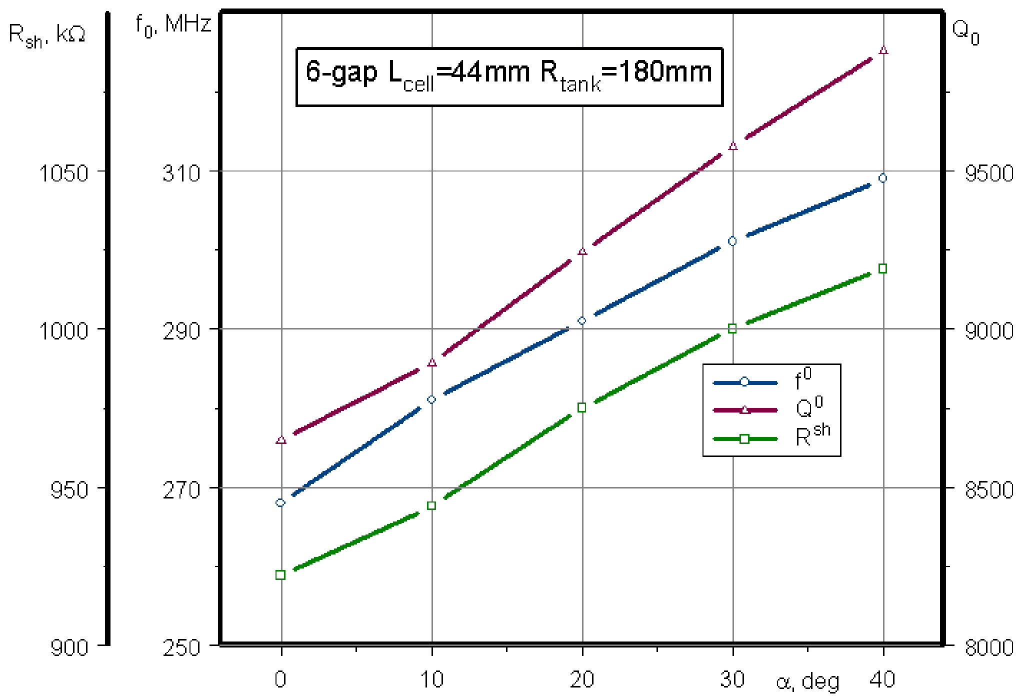

a)

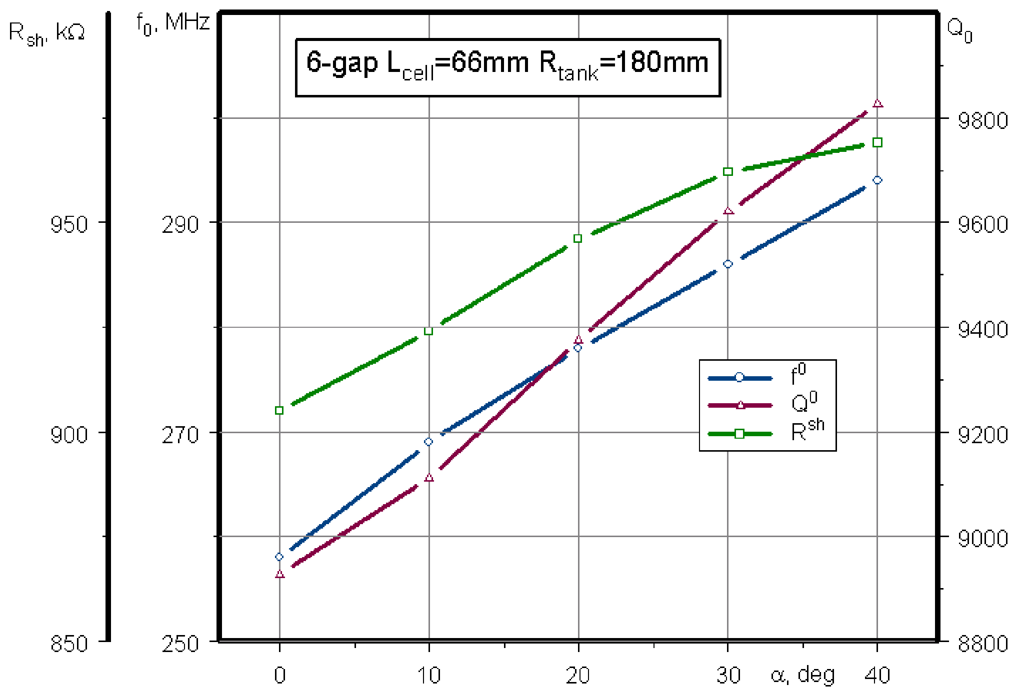

b)

Fig. 7. The calculated values of Q_0, frequency f_0, and R_{sh} versus the ridge angle α_R for IH-cavities with the tank radius R_{tank}=180 mm:

a) The 6-gap cavity with the cell length L_{cell}=44 mm;

b) The 6-gap cavity with the cell length L_{cell}=66 mm.

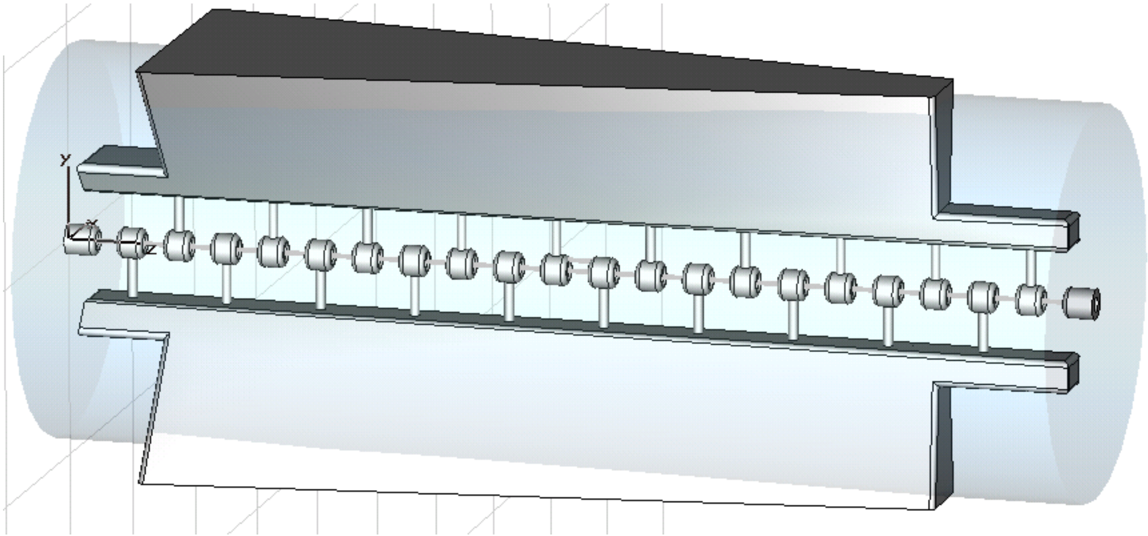

a)

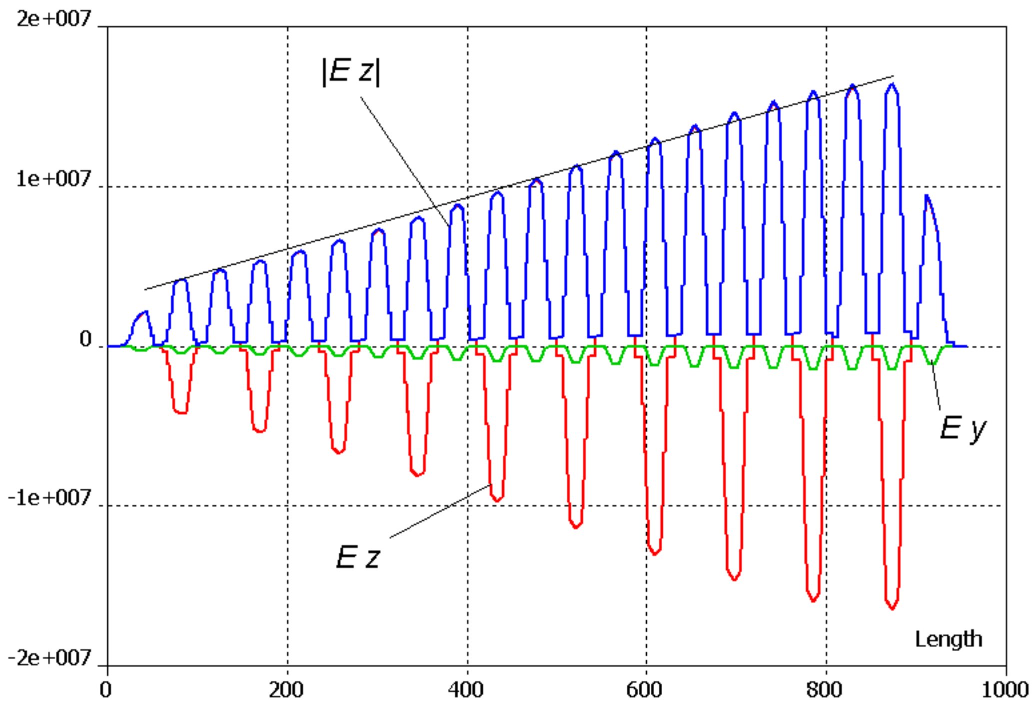

b)

Fig. 8. The IH- cavity with decreasing along the structure ridge angle α_R :

the schematic view (a) and the electrical field distribution along the structure (b).

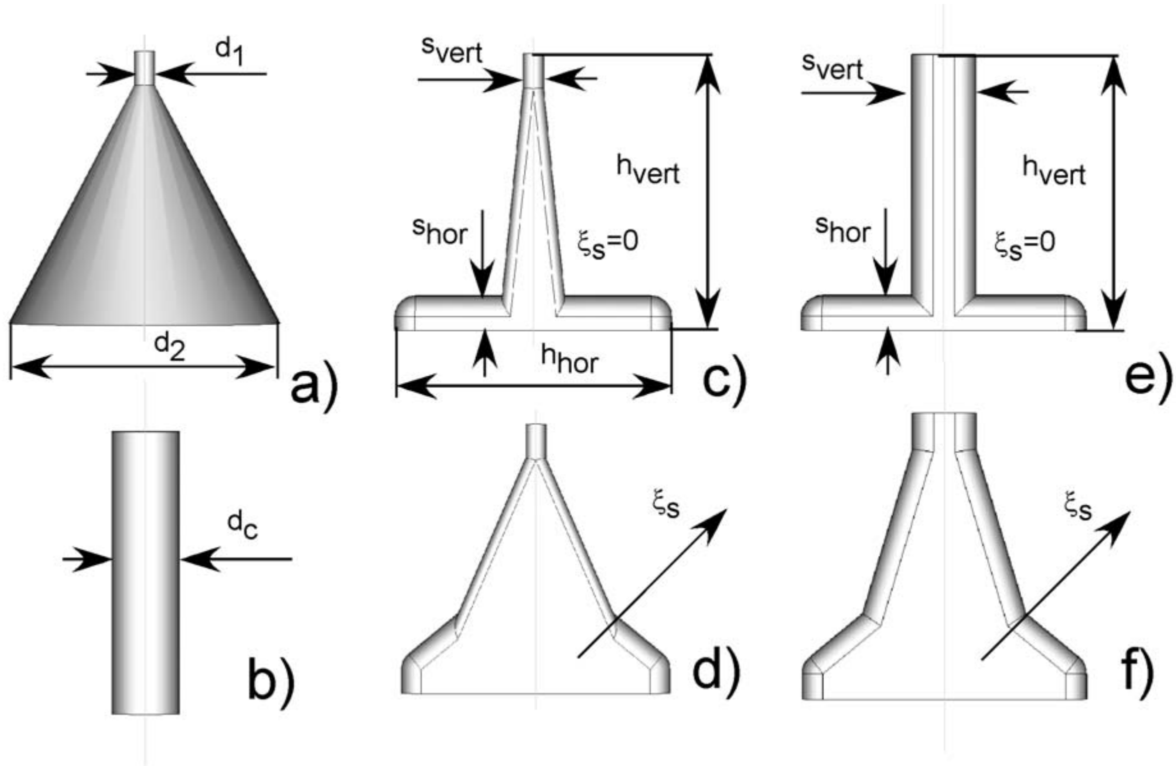

Fig. 9. The conical (a), cylindrical (b) and trianlgular stems (c-d).

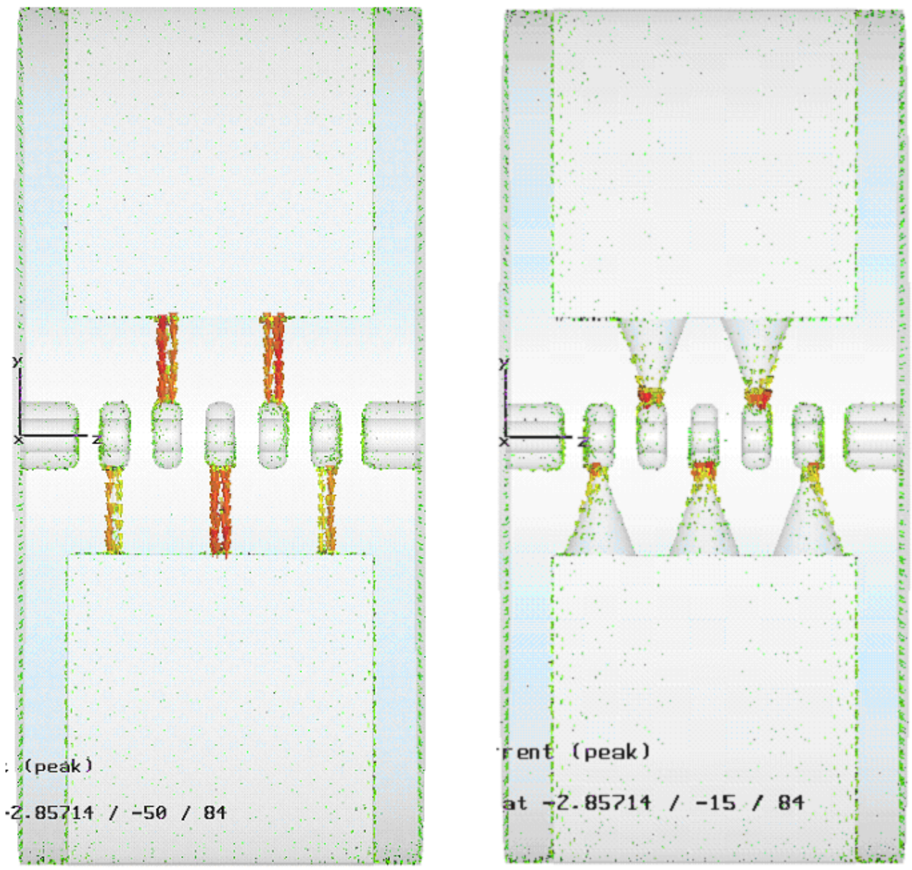

Fig. 10. The RF current distributions in IH-cavities with the cylindrical and conical stems.

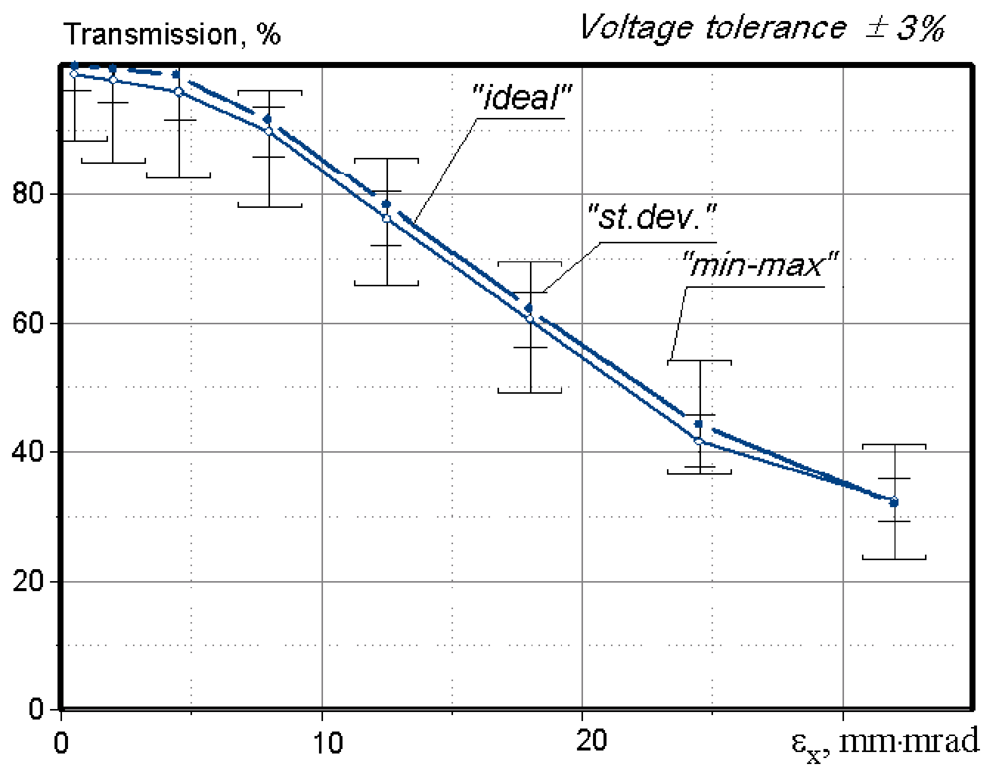

a)

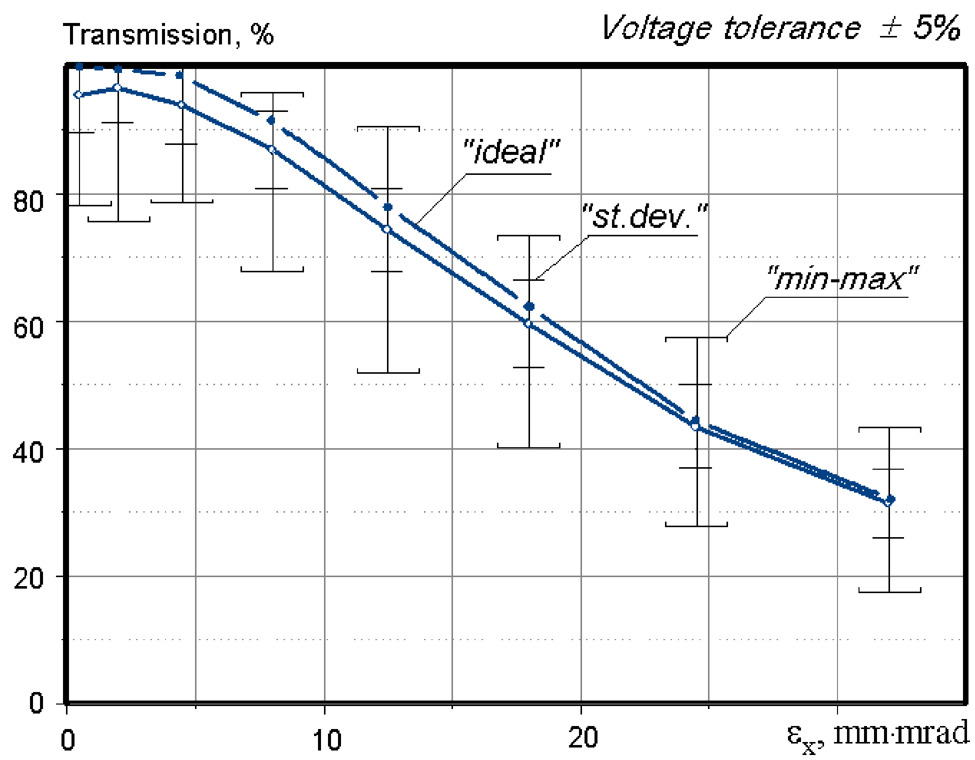

b)

Figure 11. The beam transmission versus the parameter ε_x

for the relative tolerances of the gap voltages $\delta_U = \pm 3\,\%$ (a) and $\delta_U = \pm 5\,\%$ (b).

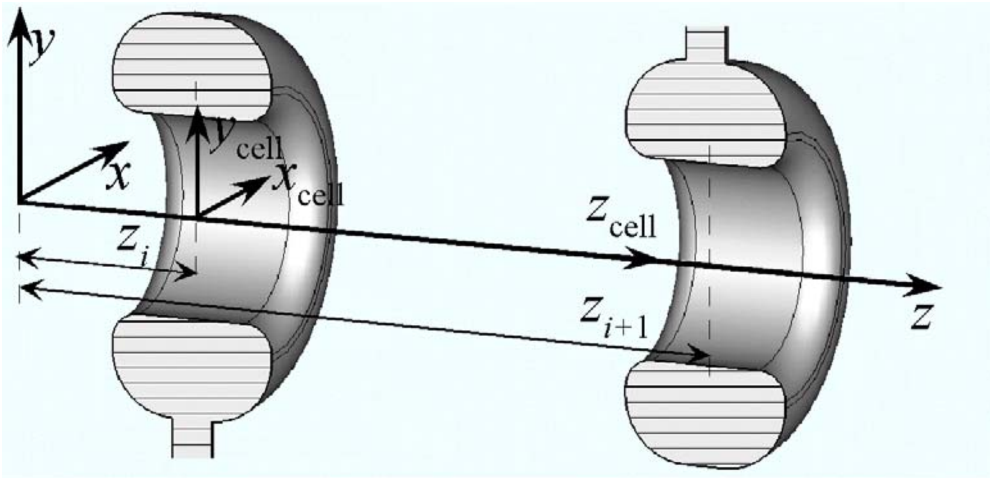

a)

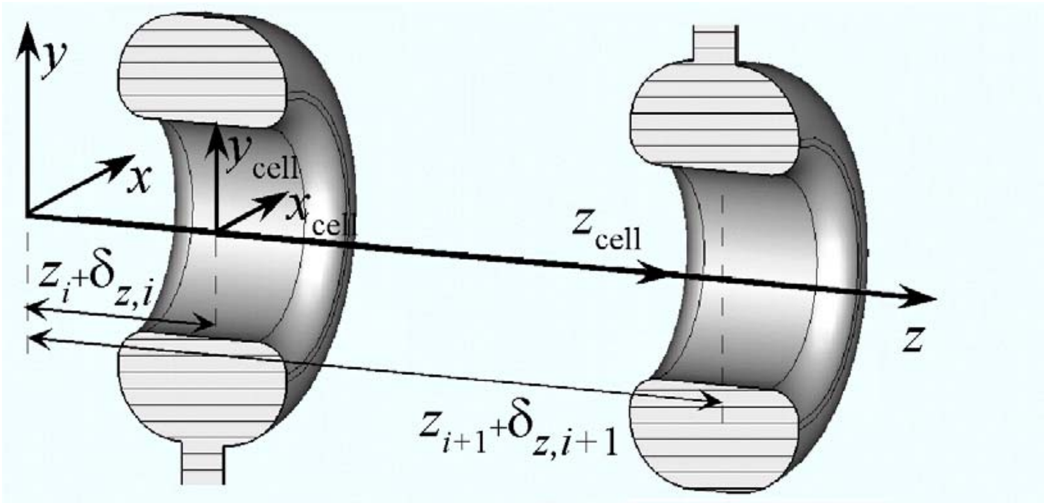

b)

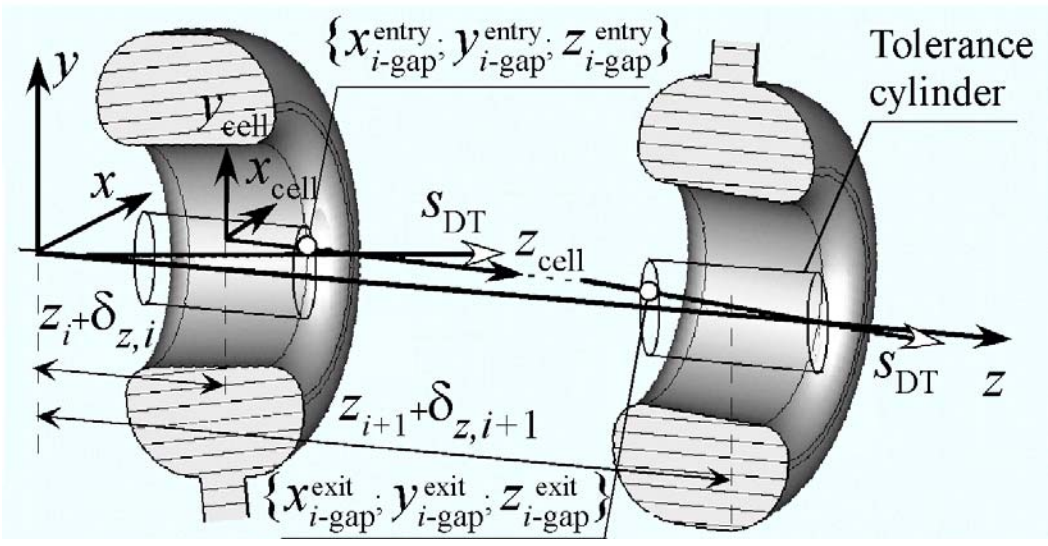

c)

Figure 12. The randomization procedure for the drift-tube geometry.

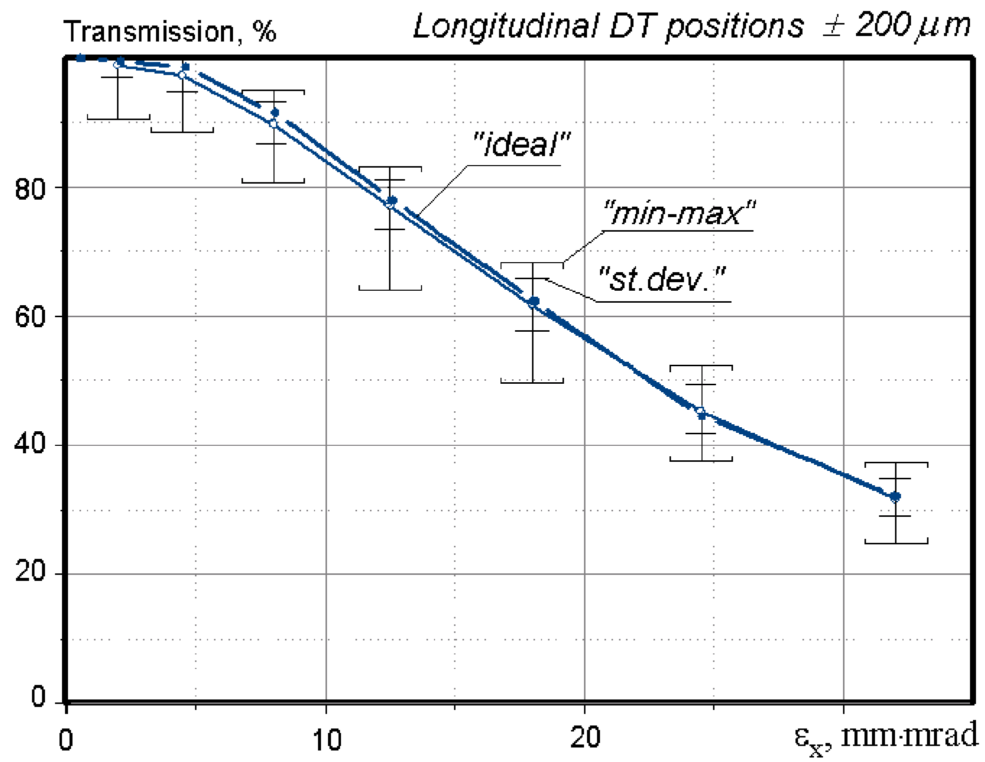

a)

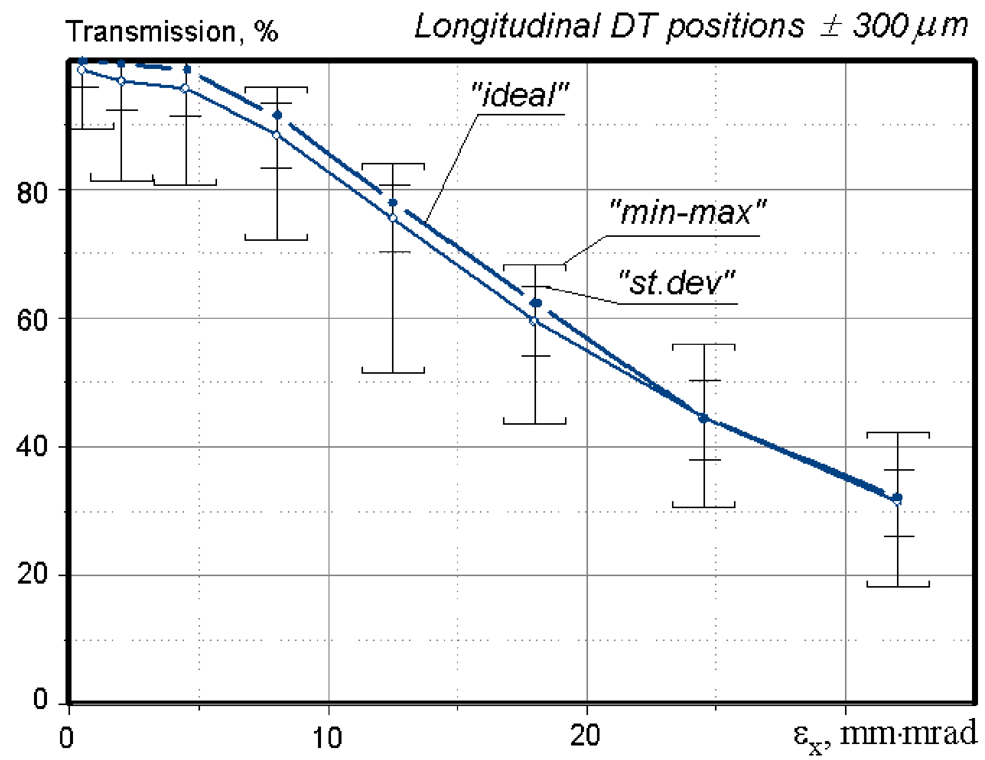

b)

Figure 13. The beam transmission versus the parameter ε_x

for the longitudinal DT tolerances $\Delta_z = \pm 200$ μm (a) and $\Delta_z = \pm 300$ μm (b).

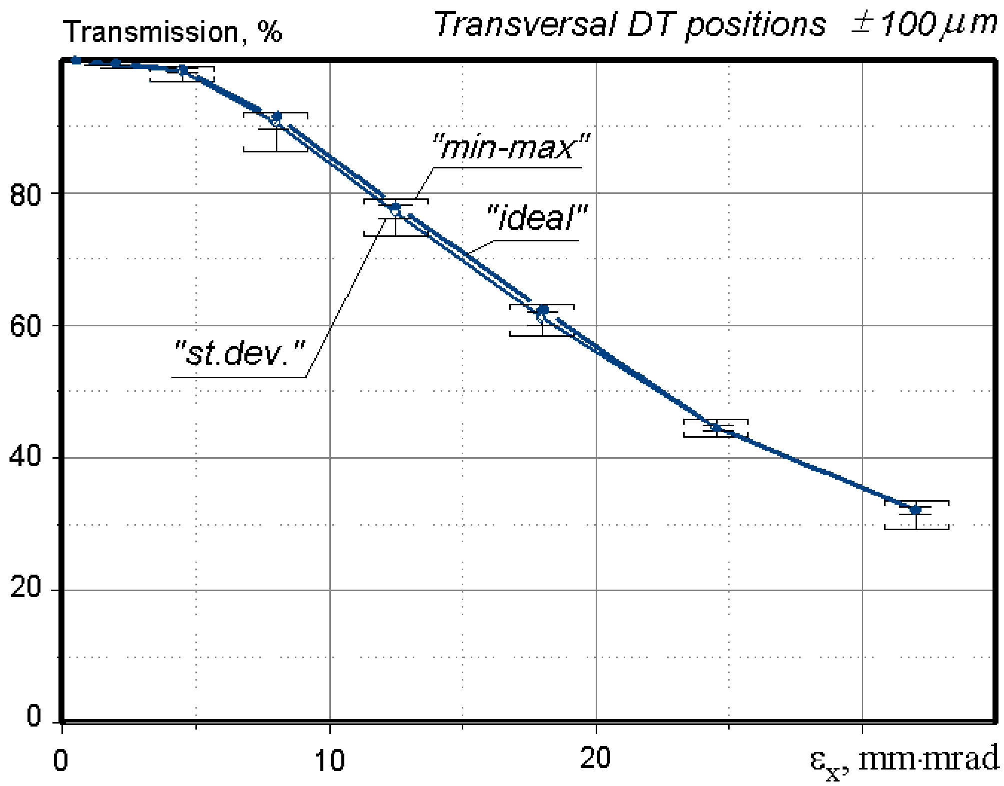

a)

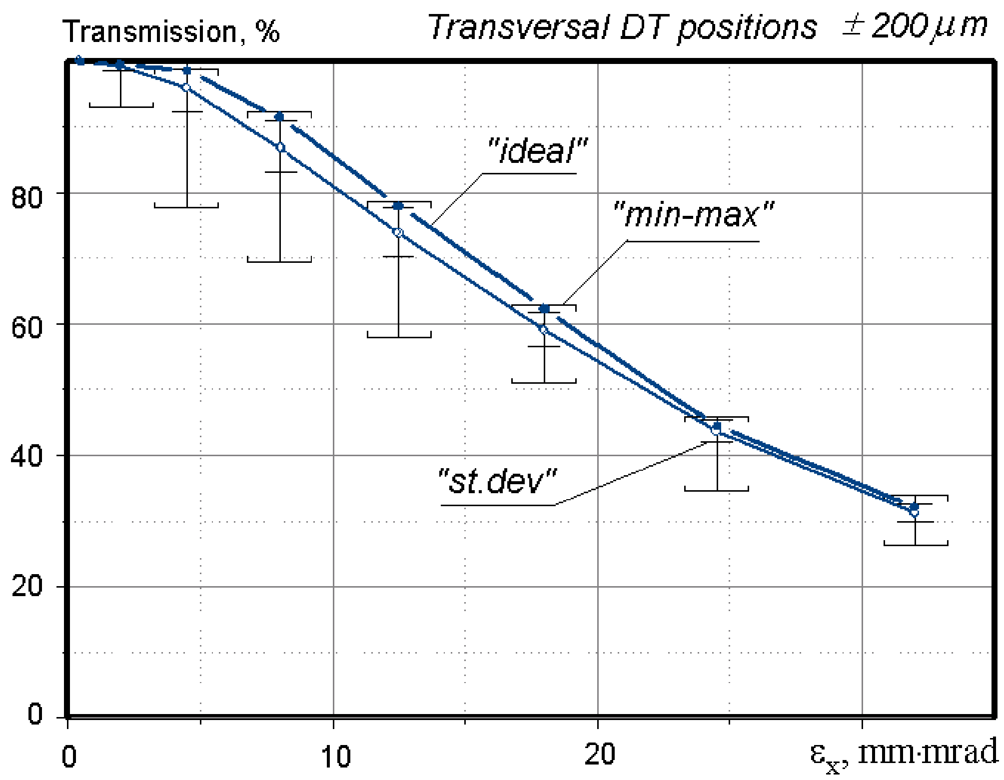

b)

Figure 14. The beam transmission versus the parameter ε_x
for the transversal DT tolerances $\Delta_r = \pm 100\ \mu\text{m}$ (a) and $\Delta_r = \pm 200\ \mu\text{m}$ (b).

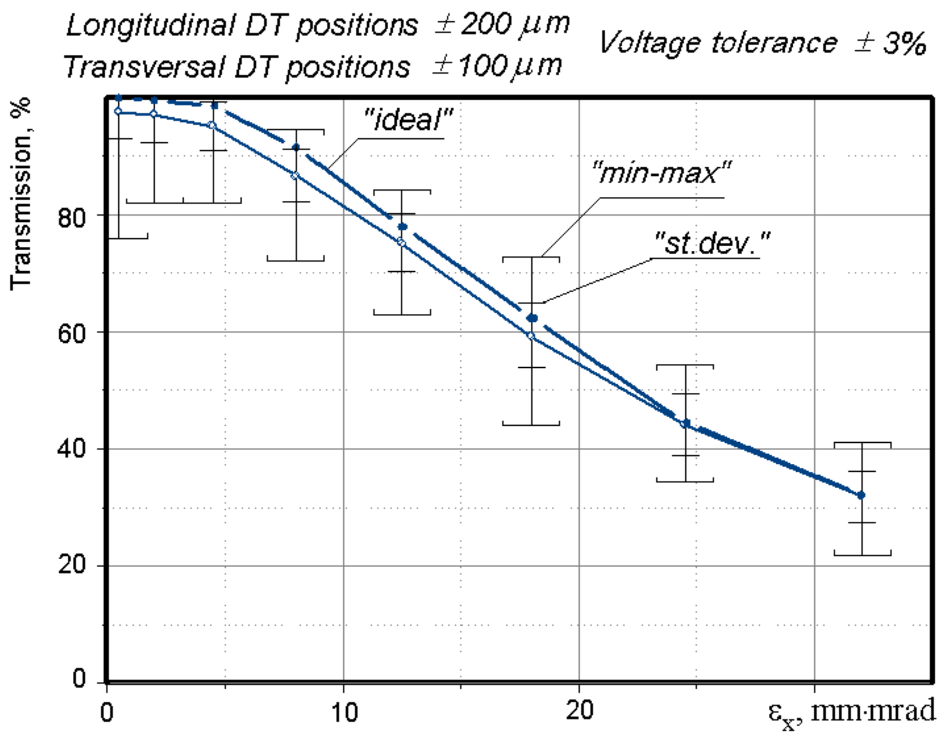

a)

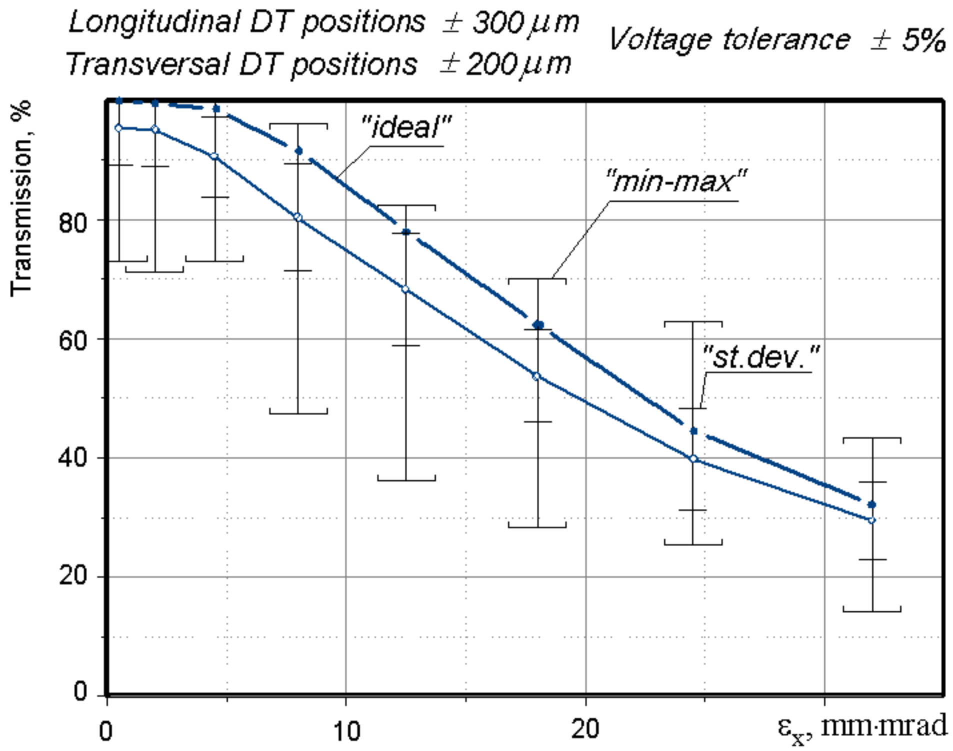

b)

Figure 15. The beam transmission versus the parameter ε_x:

a) for the tolerance set $\delta_U = \pm 3\,\%$, $\Delta_z = \pm 200\ \mu\text{m}$, and $\Delta_r = \pm 100\ \mu\text{m}$;

b) for the tolerance set $\delta_U = \pm 5\,\%$, $\Delta_z = \pm 300\ \mu\text{m}$, and $\Delta_r = \pm 200\ \mu\text{m}$;.

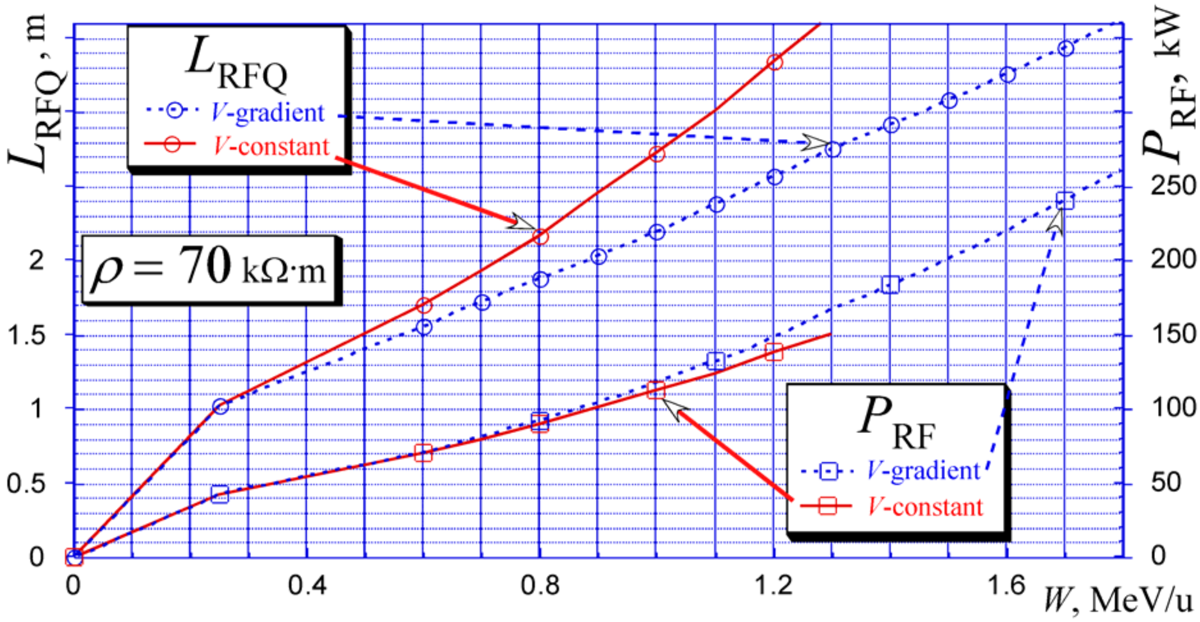

Fig. 16. The total length and the required RF power versus the energy of accelerated ions for the constant voltage RFQ and gradient-voltage RFQ.

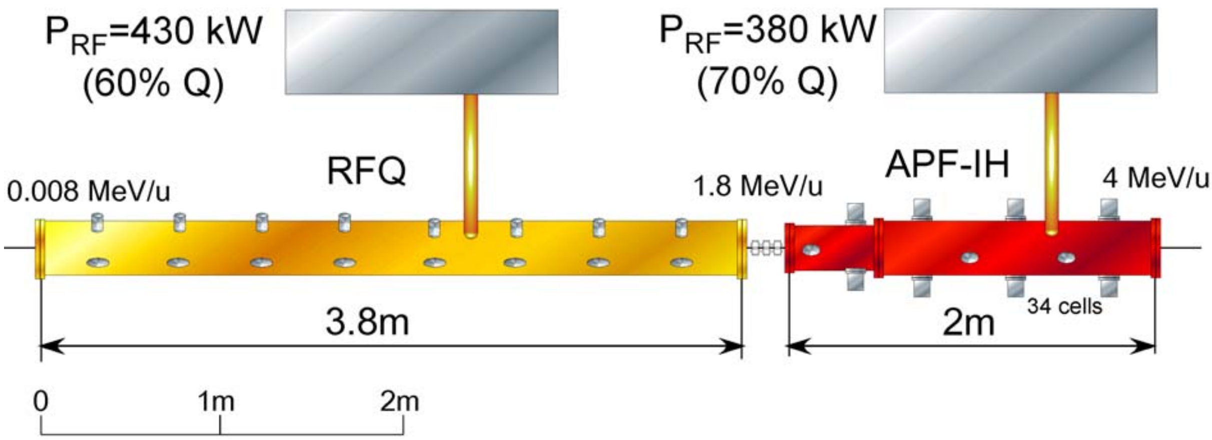

Fig. 17. The general view of the accelerator complex with the gradient-voltage RFQ.